

A Constraint on Dark Matter Self-Interaction from Combined Strong Lensing and Stellar Kinematics in MACS J0138-2155

Jackson H. O'Donnell^{*,} Tesla E. Jeltema[✉], and M. Grant Roberts[✉]

*Department of Physics, University of California, Santa Cruz
1156 High Street, Santa Cruz, CA 95064 and
Santa Cruz Institute for Particle Physics
1156 High Street, Santa Cruz, CA 95064*

James Nightingale[✉]

*School of Mathematics, Statistics,
and Physics, Newcastle University
Newcastle, NE17RU*

Abigail Flowers[✉]

*Department of Physics, University of Zürich
Zürich, Switzerland*

Dhruv Aldas[✉]

*Department of Physics, University of California, Berkeley
CA 94720*

(Dated: August 29, 2025)

Self-Interacting Dark Matter (SIDM) represents a compelling alternative to collisionless dark matter, with diverse phenomenological signals from dwarf galaxy to galaxy cluster scales. We present new constraints on the SIDM cross section from the galaxy cluster MACS J0138-2155, host to the strongly lensed supernovae Requiem and Encore. Our analysis combines strong gravitational lensing with spatially resolved stellar kinematics of the central galaxy, employing several methodological advances over previous cluster-scale SIDM studies. The result is a self-consistent measurement of the density profile of MACS J0138-2155 across two orders of magnitude in radius. Our lensing and kinematics analyses individually yield highly consistent results, and from their combination we report a 95% confidence upper limit on the SIDM cross section of $\sigma/m < 0.613 \text{ cm}^2/\text{g}$, at an interaction velocity of $\langle v_{\text{pair}} \rangle < 2090 \text{ km/s}$. This constraint, derived from the most detailed single-system analysis to date, is competitive with previous cluster-scale limits while demonstrating the power of combining complementary gravitational probes. The methodology developed here advances precision cluster lens modeling and will inform future studies of dark matter physics, as well as time-delay cosmography in this unique strong lensing system. Additionally, our results imply SN Requiem will reappear sooner than previously reported, with a 1σ CL between January 2027 and November 2028 at $H_0 = 67.7 \text{ km s}^{-1} \text{ Mpc}^{-1}$.

I. INTRODUCTION

The nature of dark matter remains one of the most significant outstanding problems in physics. An unambiguous, non-gravitational signature of dark matter has yet to be found in direct or indirect dark matter searches, nor have signs of beyond the Standard Model theories, like supersymmetry, containing dark matter particle candidates been seen. However, the growth and properties of cosmic structure place strong constraints on the nature of dark matter over a large range of scales. The model of cold dark matter (CDM), in which the dark matter particles are collisionless, has been highly successful at modeling large-scale structure and its evolution, but faces potential tensions at smaller scales like dwarf galaxies.

This and a lack of detection of CDM particle candidates motivate thinking more broadly about the properties of dark matter.

Fortunately, non-CDM models for dark matter predict potentially measurably differences in the properties of dark matter structures, including their densities, shapes, and substructure abundances. In particular, several models including self-interacting dark matter, warm dark matter, and very light dark matter predict lower central densities in dark matter halos compared to CDM.

In this paper, we focus on using the combination of strong gravitational lensing (SL) and spatially resolved stellar kinematics to constrain the dark matter density to small radii in the galaxy cluster MACS J0138.0-2155, and we motivate these choices below. In addition, the modeling presented here represents several improvements to the methodology and consistency of strong lens cluster modeling.

* jhdonnell@ucsc.edu

A. Self-Interacting Dark Matter

Self-Interacting Dark Matter (hereafter SIDM) has received intense interest in recent years, becoming one of the most well-studied alternatives to CDM. SIDM entails a simple phenomenological change to collisionless DM, in which DM particles are allowed to interact through a new force with a (possibly velocity-dependent) elastic scattering cross section. Such self-interactions are well-motivated theoretically, and arise naturally from many particle models of DM [1, 2]. A common example is a massive DM particle coupled to a light mediator through a Yukawa interaction [1, 3, 4].¹

SIDM can produce a range of different effects at different mass scales. In particular, scattering and associated heat transfer leads to the reduction of “cuspy” DM density profiles into flattened “cored” DM density profiles [5, 6]. On longer timescales, the gravothermal evolution caused by SIDM potentially leads to runaway gravothermal collapse. This evolution from core formation to core collapse naturally explains the diversity seen in dwarf galaxies; SIDM-induced core collapse could potentially even lead to the formation of supermassive black hole seeds in the early universe [7–11]. At intermediate mass scales, the effects of SIDM on halo morphology are expected to be “washed out” by baryonic effects [12, 13]. Accordingly, most constraints on SIDM come from the extreme ends of the halo mass scale: dwarf galaxies, low-surface brightness (LSB) galaxies, and galaxy clusters [2].

Currently, the most stringent absolute constraints on the SIDM cross section come from strong lensing of galaxy clusters, which suggest $\sigma/m \lesssim 0.1 \text{ cm}^2/\text{g}$ [14, 15]. Constraints on dwarf and LSB mass scales from fitting rotation curves suggest a higher value, around $O(1 - 10) \text{ cm}^2/\text{g}$ [16]. However, Roberts *et al.* [17] suggests that σ/m could be as high as $20 - 40 \text{ cm}^2/\text{g}$ at this mass scale, when SIDM-induced core collapse is accounted for. These higher cross-sections alleviate tensions associated with the diversity of dwarf rotation curves by predicting that these low-mass galaxies are in different phases of their gravothermal evolution; most will be mildly in the core-collapsed phase, while others may only just be entering this phase, and some may be more deeply core collapsed.

The discrepancy in the size of the cross-section implied by cluster and dwarf galaxy observations suggests that the SIDM cross-section must necessarily be a velocity-dependent interaction if we wish to explain dwarf rotation curves through this mechanism. It is clear that clusters can provide stringent constraints on the SIDM interaction strength at high mass scales. Therefore, to further probe the SIDM cross-section at these scales, in this paper we focus on strong lensing in galaxy clusters.

B. Cluster SIDM constraints

We aim to improve on previous SIDM constraints at cluster scales by constructing the most detailed model to date of an individual system. This work constrains the dark matter density across a wide range of radii by combining stellar kinematics of the central galaxy at small radii and observed SL features at intermediate radii. In this section we summarize previous related studies, and contrast the approach taken in this paper.

Early work along these lines aimed to differentiate between the luminous and dark matter distributions in clusters, independently using SL and stellar kinematics measured along a 1D slit [18, 19], and found the DM profile alone to be shallower than expected in a CDM cosmology. Recently, Cerny *et al.* [20] took a similar approach, combining 2D IFU kinematics with SL to model six clusters, and likewise found a DM density profile shallower than a Navarro-Frenk-White (NFW) profile. However, these studies did not translate their measurements to SIDM constraints or any other alternate cosmological model.

More recent studies explicitly constrained SIDM using similar approaches, albeit with less detailed models of larger samples. Sagunski *et al.* [14] studied a sample of 8 galaxy groups and 7 galaxy clusters, constraining their density profile by combining stellar kinematics and strong gravitational lensing. Their results show a clear preference for non-zero cross-sections, with $\sigma/m = 0.19 \pm 0.09 \text{ cm}^2/\text{g}$ at cluster scales, and $\sigma/m = 0.5 \pm 0.2 \text{ cm}^2/\text{g}$ at group scales. For both kinematics and lensing, however, they limit their analysis to simplified approximations. For stellar kinematics, they use stellar velocity dispersions in bins along a 1D slit computed previously in Newman *et al.* [19], which yielded between 3 and 8 bins per cluster. In this work, we measure stellar velocity dispersions of a central cluster galaxy in 2D, using an IFU data cube to obtain 25 spatial bins, as described in Section III C 1. Furthermore, their strong lens models are limited to reconstructing an average convergence in a certain aperture, derived from previous strong lens models of each system.

Andrade *et al.* [15] presented an SIDM constraint from 8 lensing clusters, constructing a detailed SL mass model of each system, and relating those results to the SIDM cross-section σ/m . However, they use *only* SL, without stellar kinematics to provide constraints on the innermost region. In addition, they choose a parametric cored-NFW density profile for the cluster DM halo, and relate their result to an SIDM cross-section after-the-fact. We improve on this latter choice by computing the SIDM halo density profile via the formalism described in Appendix A, and directly predicting strong lensing observables from this profile at every step.

We note that other probes exist to constrain SIDM in clusters, which do not explicitly reconstruct the DM density profile in the innermost region. These include offsets between the galaxies and dark matter in merging clusters [21], offsets between the central galaxy and the center of

¹ We stress that our results do not assume a particular form of this particle interaction.

mass [22, 23], the radial acceleration relation of members in the cluster outskirts [24], and potentially the ellipticity of dark matter haloes [25, 26]. Due to a combination of observational limitations and theoretical uncertainties, however, these constraints are not yet competitive with those from SL, such as Sagunski *et al.* [14] and Andrade *et al.* [15] described above.

C. Lensing Cluster MACS J0138.0-2155

In this work, we focus on the strong lensing galaxy cluster MACS J0138.0-2155 (hereafter MACSJ0138). We leverage its deep, publicly-available data to constrain the inner density profile of its dark matter halo. This lensing cluster is of particular interest to cosmology: one of the first known strongly lensed supernovae, known as “SN Requiem”, was discovered in archival HST imaging of this system [27]. More recently, JWST observations of this system discovered a *second* strongly lensed supernova, named “SN Encore” [28], making this the first known lens system to host multiple strongly-lensed SNe. As a unique, highly interesting system, MACSJ0138 has been the subject of extensive astronomical observations. We describe the data used in this analysis in Section II.

Furthermore, MACSJ0138 is a very “clean” system, ideal for constraining its halo’s inner density profile. It is known to be a relaxed, non-merging cluster, whose primary lensed source is a bright, quiescent galaxy at redshift 1.95. This source appears in at least 5 separate images, surrounding the cluster’s center; furthermore, X-ray data show it to be a relaxed system, exhibiting close to spherical symmetry [29].

Here we briefly summarize previous studies on MACSJ0138. Multiple spectroscopic studies have been done on the dynamical state of the cluster and its member galaxies [29, 30], and the quiescent source hosting SNe Requiem and Encore [28, 31–33]. The strong lensing observed in MACSJ0138 has been modeled previously by Newman *et al.* [32], which reported spectroscopic redshifts of the lens and source, and Rodney *et al.* [27], which presented the discovery of SN Requiem. We confirm the redshifts presented in both papers using the IFU data described in Section II B. More recent mass models leveraging deeper data on this system were published in Ertl *et al.* [34] and Acebron *et al.* [35]. We compare the results presented in this work with the latter two papers in Section V A.

II. DATA

The data used in this work includes space-telescope imaging and ground-based spectroscopy which are described below.

A. High-resolution Imaging

MACSJ0138 has received extensive high-resolution imaging from both HST and JWST. MACSJ0138 was first observed by HST in 2016 (Proposal ID 14496, PI A. Newman). These observations included three instrument/filter combinations: ACS/WFC band F555W, and WFC3/IR bands F105W and F160W. SN Requiem was later identified in these observations [27]. In 2019, MACSJ0138 was observed again by HST as part of the REQUIEM program (Proposal ID 15663, PI M. Akhshik). These observations utilized WFC3 exclusively, using the UVIS channel with filters F814W and F390W, and the IR channel with filters F110W, F125W, and F140W.

Following the discovery of SN Encore in November 2023, a JWST director’s discretionary time program (JWST-GO-6549, PI J. Pierel) was approved to monitor SN Encore. This program observed MACSJ0138 in three epochs between December 5 2023, and January 8 2024. During each epoch, MACSJ0138 was observed by NIRCam using six filters: F115W, F150W, F200W, F277W, F356W, and F444W. We utilize the WFC3/IR imaging from Program 14496 to measure the observed positions of SN Requiem. To measure observed positions of other features in the lensed source, as well as SN Encore, we utilize JWST NIRCam imaging in bands F115W, F150W, and F200W from Program JWST-GO-6549.

B. MUSE Spectroscopy

The Multi Unit Spectrographic Explorer (MUSE) is a second-generation integral field spectrograph on the VLT [36]. MACSJ0138 received three MUSE pointings of 970s each during Period 103, through Program 0103.A-0777(A). These observations used MUSE in wide-field mode, which has a field-of-view of approximately $1' \times 1'$, without adaptive optics. In this work, we utilize the reduced data cube of these observations obtained from the ESO data archive, processed by ESO pipeline version `muse/2.8` [37].

III. MODELING METHODS

In this work, we self-consistently model and constrain the density profile of the dark matter halo of MACSJ0138, using both stellar kinematics and strong lensing, combining complementary constraints of the DM density profile at $\sim 1 - 20$ kpc, and ~ 100 kpc, respectively. Central to this work is providing a coherent model for the 3D density of the overall DM halo, modified by the effects of SIDM. This shared mass model used by both the strong lensing and stellar kinematics probes is described in Section III A. Next, Section III B describes how we construct a strong lensing mass model, and fit it to observed strong lensing features, including handling

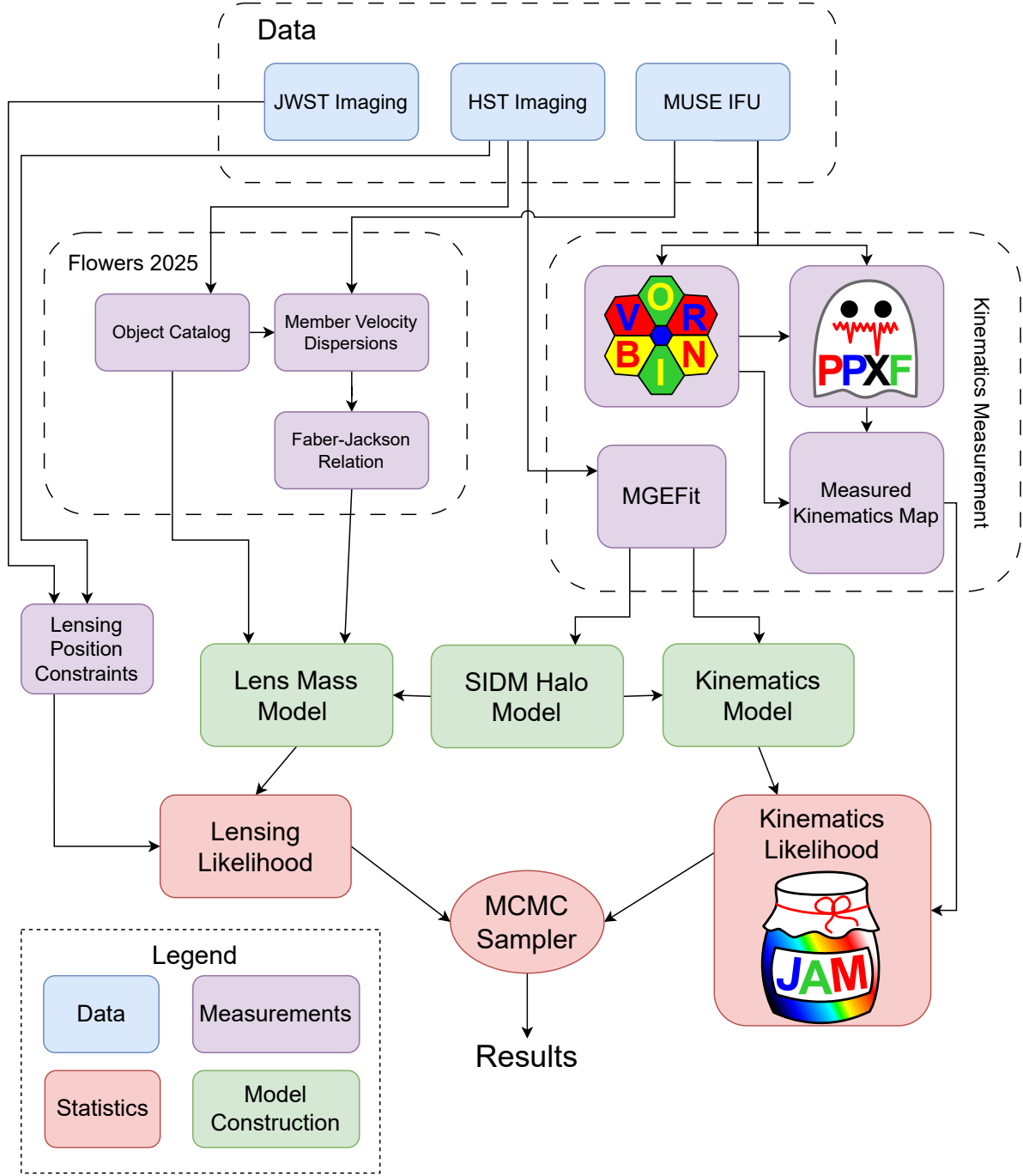


FIG. 1. **Analysis Outline:** High-level overview of the analysis done in this work. Pieces of this analysis were presented in Flowers *et al.* [29]. Lens modeling is accomplished with PyAutoLens [38, 39], and the kinematics modeling in this work uses vorbin [40], ppxf [41, 42], MGEfit [43], and JAM [44, 45].

of the contribution of cluster member galaxies, and how strong lensing observables are computed for the SIDM-modified halo. Finally, the measurement and modeling of the central galaxy’s kinematics are described in Section III C. In addition, a high-level overview of the steps in this work is provided by the diagram in Figure 1.

A. Shared SIDM Mass Model

We construct a self-consistent mass model of the dark and baryonic matter of MACSJ0138 across the regions probed by stellar kinematics and strong lensing. To represent the effect of self-interactions on the overall DM

halo of MACSJ0138, we utilize the isothermal Jeans method (see Appendix A for details), as used by previous constraints on SIDM in clusters [14, 15]². In contrast to previous work such as Andrade *et al.* [15], which constrained a parametric density profile and only related this constraint to SIDM after-the-fact, we compute the SIDM-predicted density profile at every step and consistently model both stellar kinematics and strong lensing observables directly from this profile. The SIDM-modified profile is predicted using the well-known isothermal Jeans formalism introduced in [46], as previous studies of SIDM in clusters have done [14, 15]. This semi-analytic method consists of a simple modification of an NFW DM density profile, where a boundary is drawn at a spherical radius r_1 , and all DM within r_1 is assumed to be isothermal. This boundary is conventionally defined as the radius at which DM particles have experienced, on average, one scattering over the lifetime of the halo:

$$1 = \left\langle \frac{\sigma v}{m} \right\rangle \rho_{\text{dm}}(r_1) t_{\text{halo}} \quad (1)$$

Where $\left\langle \frac{\sigma v}{m} \right\rangle$ represents the velocity-weighted SIDM cross section per particle mass, and t_{halo} is the age of the halo. This simple formalism has been shown to effectively capture the ‘core formation’ behavior of SIDM on cluster scales; see [47] for a detailed study. Our implementation of the isothermal Jeans method is described in Appendix A, including the handling of priors on r_1 and σ/m , and the effect stellar density profile. Alongside this paper, we present our open-source code for computing the SIDM density profile with this method, available at github.com/jhod0/sidm_halos.

The baryon contribution in the innermost part of the halo is essential to both accurately computing the predicted SIDM profile, and predicting strong lensing and kinematics observables. In this work we consider the impact of the stellar mass of the BCG. The light profile of the BCG is approximated as a Multi-Gaussian Expansion (MGE), as described in Section III C 3, and the baryonic mass is derived with a stellar mass-to-light ratio. We use `kcorrect` [48] version 5.1.3 to compute the V-band absolute magnitude of the BCG using Legacy Survey photometry in the g, r, i, and z bands [49]; in addition, `kcorrect` provides an estimate of the stellar mass-to-light ratio Υ_* . This yields a V-band absolute luminosity of $4.94 \times 10^{11} L_\odot$ with a corresponding $\Upsilon_{*,V}$ of 2.05. We note this is similar to the result in Newman

et al. [18], which similarly studied BCGs of lensing clusters and found $\Upsilon_{*,V}$ between 1.8 and 2.32 across seven systems. It is well known that there is considerable uncertainty on the true mass-to-light ratio, which is highly dependent on the assumed initial mass function (IMF) [14, 19]. As such, and following Sagunski *et al.* [14], we use a wide prior on $\log \Upsilon_*$ with a scatter of 0.3 dex.

Additionally, we allow for a prolate overall DM halo in three dimensions, rather than simply ellipticity in the plane of the sky. This treatment of the ellipticity introduces three parameters: the prolate axis ratio q_{3d} , the angle between the halo’s axis of symmetry and the line of sight $\cos i$, and a position angle ϕ of the apparent ellipticity in the plane of the sky. We introduce ellipticity to the overall halo while ensuring that the mass and concentration of the halo are preserved, and analytically project this prolate halo into an elliptical surface density in the plane of the sky. A detailed explanation can be found in Appendix B.

1. Shared Model Parameters

There are thus seven parameters common to both the strong lensing and kinematics models. Together, they describe the overall dark matter halo and inner baryon density profile. They are:

- $\log_{10} M_{200m}$: The overall mass of the cluster’s DM halo, defined as the mass within radius r_{200m} such that the mean density within r_{200m} is 200 times the mean matter density of the universe;
- c_{200m} : The corresponding concentration of the cluster’s DM halo;
- $\log_{10} r_1$: The radius within which DM particle self-interactions modify the DM density profile;³
- Υ_* : The stellar mass-to-light ratio of the central galaxy;
- q_{3d} : The 3D axis ratio of the cluster halo;
- $\cos(i)$: The *cosine* of the inclination angle relative to LOS;
- ϕ : The position angle of the projected, 2D ellipticity on the sky.

B. Strong Lens Modeling

Lens modeling in this work is done with the flexible open-source package `PyAutoLens` [38, 39, 50]. In addition to the built-in functionality of `PyAutoLens`, we implement several extensions to describe our lens model and

² We note that while this method only describes the ‘core-expansion’ phase of SIDM, and fails to describe ‘core-collapse’ behavior, current constraints already rule out SIDM-induced ‘core-collapse’ at cluster scales. A simple estimate based on the relation in Outmezguine *et al.* [7] predicts that a cluster like MACSJ0138 would experience ‘peak core’ (i.e., the core-expansion/core-collapse phase transition) and begin collapsing after 216 Gyr of evolution at an SIDM cross section of $0.1 \text{ cm}^2/\text{g}$ or 22 Gyr at a cross section of $1.0 \text{ cm}^2/\text{g}$.

³ Though we sample r_1 rather than σ/m , likelihoods are weighted to enforce a flat prior on $\ln(\sigma/m)$. See Appendix A.

constraints. The mass model used in this work, and the functionality implemented to enable it, are described in Section III B 1; the strong lensing constraints, and the likelihood implemented in this work, is described in Section III B 2.

1. Mass Model

Our strong lensing mass model takes a similar approach to the widely-used `lenstool` software [51, 52]. It contains two primary components: one dark matter halo for the cluster as a whole, and a set of dPIE[53] profiles representing all member galaxies, save for the central galaxy.

To represent the former, we approximate our SIDM-modified DM density profile via a sum of Cored Steep Ellipsoids (CSEs), as proposed by Oguri [54]. This CSE decomposition is computed by the `scipy` method `least_squares`, using the NFW approximation in Table 1 of Oguri [54] as an initial value. The position of the overall halo is allowed to vary slightly, with a Gaussian prior centered on the known BCG center.

In order to model the member galaxies, we implement a dPIE density profile in `PyAutoLens`. The mass of these member galaxies are all scaled by their photometry using the Faber-Jackson relation, described below; we additionally leverage a direct measurement of the Faber-Jackson relation in MACSJ0138, as advocated by Bergamini *et al.* [55]. This measurement was previously reported in Flowers *et al.* [29], yielding a slope of $\alpha \sim 0.26 \pm 0.06$ at a reference velocity dispersion of ~ 220 km/s. We note that while this measurement was done using the older, shallower MUSE data, an independent team reported a similar measurement of the Faber-Jackson relation in MACSJ0138 using the newer, deeper MUSE observations. These results, published in Granata *et al.* [30], used different methodology on different data, yet yielded the highly consistent measurement of $\alpha \sim 0.25 \pm 0.05$. Both results suggest a slightly shallower slope than those reported for three clusters in Bergamini *et al.* [55].

The dPIE profiles of the member galaxies are parameterized by their velocity dispersion σ_i , core radius $r_{a,i}$, and scale (or ‘cut’) radius $r_{s,i}$. Except where otherwise noted, all member galaxies receive a fixed core radius of 0.15 kpc. Their velocity dispersions and cut radii are scaled in the conventional way, as in [51] and [55]:

$$\sigma_{\text{LT},i} = \sigma_{\text{LT,ref}} \left(\frac{L_i}{L_0} \right)^\alpha \quad (2)$$

$$r_{s,\text{LT},i} = r_{s,\text{LT,ref}} \left(\frac{L_i}{L_0} \right)^\beta \quad (3)$$

Here, LT denotes the fiducial parameterization used in `lenstool`, rather than observed quantities. If the total mass-to-light ratio Υ_i^{tot} for these galaxies scales as L_i^γ , then $\beta = \gamma - 2\alpha + 1$. Following both Bergamini *et al.* [55] and Acebron *et al.* [35], we fix $\gamma = 0.2$. The

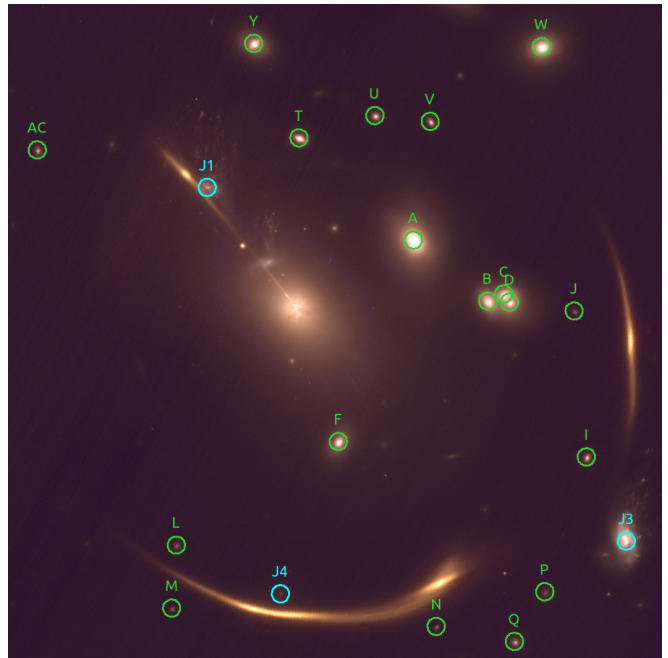


FIG. 2. JWST NIRCам imaging of MACSJ0138. All galaxies labeled here included as components of the strong lensing mass model. Red-sequence galaxies are shown in green, emission-line galaxies are in cyan. All circles have radius $0.5''$. Several cluster members outside this FOV are also included in the mass model. In this RGB image, the blue, green, red channels show the F115W, F150W, and F200W NIRCам filters, respectively.

fiducial dPIE velocity dispersion, σ_{LT} , is known to differ from observed aperture-averaged velocity dispersions σ_{ap} ; in the limit $r_a \rightarrow 0, r_s \rightarrow \infty$, the dPIE becomes an SIS, and $c_p = \sigma_{\text{ap}}/\sigma_{\text{LT}} = \sqrt{3/2}$ [53]. In practice, c_p is generally closer to unity. Bergamini *et al.* [55] provides a practical treatment of c_p in three lensing clusters with measured Faber-Jackson relations, they find that for all three clusters, given physical values of r_a and r_s , $c_p \approx 1.12$. For our priors on the substructure scaling relations in MACSJ0138, we therefore adjust the measured Faber-Jackson relation from [29] by $c_p = 1.12$.

Red-sequence cluster members included in the mass model are chosen from the catalog introduced in Flowers *et al.* [29], all of which are spectroscopically confirmed to lie at or near the cluster’s redshift.⁴ In addition, several emission-line galaxies near the cluster redshift lie close to the observed lensing features, and their mass contributions are necessary to construct a precision mass model. We include three of these in our mass model, as shown in Figure 2; note that we label these following the convention in Gibson *et al.* [56], which differs from that in

⁴ There exists a small subset of red-sequence galaxies at higher redshift, with a velocity offset of $\sim 8,000$ km/s relative to MACSJ0138 [29, 30].

Rodney *et al.* [27] and Acebron *et al.* [35]. The fourth galaxy studied in [56], J2, is not included in our mass model: its projected position is so close to the cluster center that its contribution to the observed lensing is dwarfed by the BCG and cluster DM halo.

Our lensing model includes one further component, a constant ‘external shear’ γ_{ext} across the MACSJ0138 field. This shear is parameterized by the two conventional components (γ_1, γ_2) , where γ_1 shears in the vertical and horizontal directions, and γ_2 shears along the diagonals. Acebron *et al.* [35] likewise includes a γ_{ext} component to improve their mass model, however Ertl *et al.* [34] models MACSJ0138 using two halo components without γ_{ext} . A discussion of our γ_{ext} result and its interpretation can be found in Section IV D.

2. Lensing Constraints

Our lensing mass model is constrained by a variation of the conjugate point method, computed in the source plane. For each observed source feature F , observed at multiple positions θ_i^F , the image-plane uncertainties are ellipsoids described by the covariance matrix Σ_i^F . For a given mass model, the corresponding source-plane positions and covariance are:

$$\beta_i^F = \theta_i^F - \alpha(\theta_i^F) \quad (4)$$

$$B_i^F = A(\theta_i^F) \Sigma_i^F A^T(\theta_i^F) \quad (5)$$

Where $A(\theta)$ is the lensing Jacobian at image plane position θ . Given these predicted source plane positions, we analytically marginalize over the unknown intrinsic source plane position for each feature. In practice, to avoid overfitting to critical curves of the lens model, we average B_i^F across all image-plane positions within the uncertainty ellipsoid described by (θ_i^F, Σ_i^F) . For each set of observed features F , this yields a best-fit source plane position $\hat{\beta}^F$, with corresponding uncertainty ellipsoid \hat{B}^F , and a likelihood \mathcal{L}^F :

$$\hat{\beta}^F = \hat{B}^F \left(\sum_i (B_i^F)^{-1} \beta_i^F \right) \quad (6)$$

$$(\hat{B}^F)^{-1} = \sum_i (B_i^F)^{-1} \quad (7)$$

$$\begin{aligned} \log \mathcal{L}^F = & -\log \sqrt{\frac{|\hat{B}^F|}{2\pi}} \\ & -\frac{1}{2} \sum_i (\beta_i^F - \hat{\beta}^F)^T (\hat{B}^F)^{-1} (\beta_i^F - \hat{\beta}^F) \end{aligned} \quad (8)$$

This likelihood is implemented as an extension of `PyAutoLens`. This method was later found to be equivalent to that introduced in Section 5.1 of Lombardi [57].

Our constraints include features in all five arcs of the primary quiescent source. Although recent work has reported additional sources from faint emission lines in

deep MUSE data[30], those sources are not used in this work. All position constraints are measured from JWST NIRCcam imaging, save for three observed images of SN Requiem, which was only seen at an earlier epoch. The positions of the three SN Requiem images are taken from Rodney *et al.* [27], and assigned a higher position uncertainty due to the lower resolution of HST imaging. The position constraints used here are shown in Figure 3, and listed in Table I.

C. Stellar Kinematics of the BCG

Stellar kinematics of SL deflectors provides a powerful, independent probe of the lensing mass distribution, especially if it can be resolved spatially. Early work along these lines used slit spectra of central cluster galaxies to measure variations in the stellar velocity dispersions in one dimension [18, 19, 58]. Much recent work has leveraged IFU spectra to study the dynamics of lensed systems, including lensed quasar systems [59–61], time delay constraints on the Hubble constant [62, 63], galaxy-scale multi-source-plane lenses [64], and even a group-scale strong lens [65, 66]. In the majority of these studies, the primary contribution of the stellar dynamics is to refine the strong lensing model, yielding a more accurate result and potentially breaking the mass-sheet degeneracy. In our case, however, the inner density profile constrained by central galaxy’s dynamics is of direct scientific interest: SIDM affects the halo’s dark matter density in precisely this region.

Here we describe the procedure for measuring spatially resolved stellar kinematics, and how it is used to constrain our mass model. Sections III C 1 and III C 2 describe how the kinematics map was measured and validated; Section III C 3 describes the light profile of the central galaxy, essential to modeling the kinematics; and Section III C 4 describes how our mass model is constrained by this data.

1. Measuring the Kinematics Map

To robustly measure the stellar kinematics in numerous spatial bins across the central galaxy, we take a similar approach to Shajib *et al.* [59]. We consider all IFU ‘spaxels’ along the central galaxy, binning them spatially using `vorbin`[40] such that each bin attains a target spectral signal-to-noise. We use all pixels within an ellipse tracing the BCG, with a major axis of 8.5” and a minor axis of 5”. Two circular regions are excluded due to contamination by other galaxies along the line of sight. These spectra are spatially binned to a target signal-to-noise of 23/Å between the rest-frame wavelengths of 5035 and 5160Å, just below the Mg b absorption feature. This yields 25 spatial bins, as shown in Figure 4.

Spectral fitting is done with the widely used software package `ppxf`[41]. This tool requires a set of input tem-

Feature Label	RA	Declination	Semi-Major Axis	Semi-Minor Axis	Position Angle
bulge.1	01:38:03.93	-21:55:49.23	0.91''	0.13''	75.69°
bulge.2	01:38:03.17	-21:55:47.69	0.58''	0.11''	-63.68°
bulge.3	01:38:02.38	-21:55:33.68	0.47''	0.11''	4.55°
bulge.4	01:38:04.23	-21:55:24.07	0.43''	0.17''	46.12°
bulge.5	01:38:03.80	-21:55:31.09	0.12''	0.07''	41.44°
SN-E.1	01:38:03.75	-21:55:49.66	0.1''	—	—
SN-E.2	01:38:03.17	-21:55:47.85	0.1''	—	—
SN-R.1	01:38:03.63	-21:55:50.40	0.15''	—	—
SN-R.2	01:38:02.96	-21:55:47.23	0.15''	—	—
SN-R.3	01:38:02.42	-21:55:38.43	0.15''	—	—
A.1	01:38:03.48	-21:55:50.29	0.1''	—	—
A.2	01:38:03.13	-21:55:48.74	0.1''	—	—
A.3	01:38:02.40	-21:55:38.62	0.1''	—	—
B.1	01:38:03.65	-21:55:50.16	0.1''	—	—
B.2	01:38:03.08	-21:55:47.92	0.1''	—	—
B.3	01:38:02.39	-21:55:37.15	0.1''	—	—
C.1	01:38:03.89	-21:55:49.67	0.1''	—	—
C.2	01:38:03.06	-21:55:47.31	0.1''	—	—
F.1	01:38:04.04	-21:55:48.83	0.1''	—	—
F.2	01:38:03.10	-21:55:47.12	0.1''	—	—
G.1	01:38:04.16	-21:55:48.20	0.1''	—	—
G.2	01:38:03.07	-21:55:46.46	0.1''	—	—
G.3	01:38:02.40	-21:55:32.20	0.1''	—	—
H.1	01:38:04.17	-21:55:47.86	0.1''	—	—
H.2	01:38:03.14	-21:55:46.76	0.1''	—	—
H.3	01:38:02.40	-21:55:30.69	0.1''	—	—
J.1	01:38:04.10	-21:55:48.16	0.1''	—	—
J.2	01:38:03.20	-21:55:47.23	0.1''	—	—
J.3	01:38:02.39	-21:55:30.96	0.1''	—	—

TABLE I. **Position constraints:** The constraints used for the strong lensing mass model. Each group of observed features is given a separate label (e.g. ‘SN-E’, ‘A’), and each separately observed position is given a number (‘SN-E.1’, ‘A.2’). Position angles are given east-of-north.

plates, and an optimal combination of templates is found which closely represents the user’s spectrum. In this work, we use the X-Shooter Library (XSL) Data Release 3[67], a set of 830 spectra of 683 diverse stars, as our template library. All template spectra are normalized by their mean flux between 4000Å and 4200Å. To exclude low-quality spectra, the mean SNR per pixel in this region is computed, and template spectra with SNR less than one are excluded. This is similar in spirit to the “cleaning” advocated by Knabel *et al.* [61].

We compute maps of the stellar kinematics in each Voronoi bin as follows. First, the spectrum of the entire BCG is extracted (i.e., all IFU ‘spaxels’ in all Voronoi bins). Then `ppxf` is run once on this total spectrum, and provided as templates the XSL stellar spectra described above. An example of this result is shown in Fig 16. This fit determines a linear combination of XSL template spectra which most closely matches our observed spectrum; we record this combination as the *optimal template*. Next, for each Voronoi region, `ppxf` is applied to

the region’s spectrum, this time using the single optimal template for the stellar component rather than providing a library of templates. For each spectral fit, we allow `ppxf` to fit velocity moments to the 4th order, meaning we allow for nonzero values of the third- and fourth-order moments h_3 and h_4 ⁵.

We note that this central galaxy exhibits strong emission lines, potentially associated with an AGN and star formation. As such, we provide a list of emission line templates to `ppxf` in order to obtain the highest quality spectral fit. All emission lines are associated with a single kinematic component, separate from the stellar component. We include all emission lines in the relevant wavelength range known by `ppxf`, and manually add three lines not known by `ppxf`: [SII] 4069Å, FII 5198Å, and [NI] 5201Å. While the kinematics of this gas com-

⁵ See Cappellari and Emsellem [41] for an explanation of these moments.

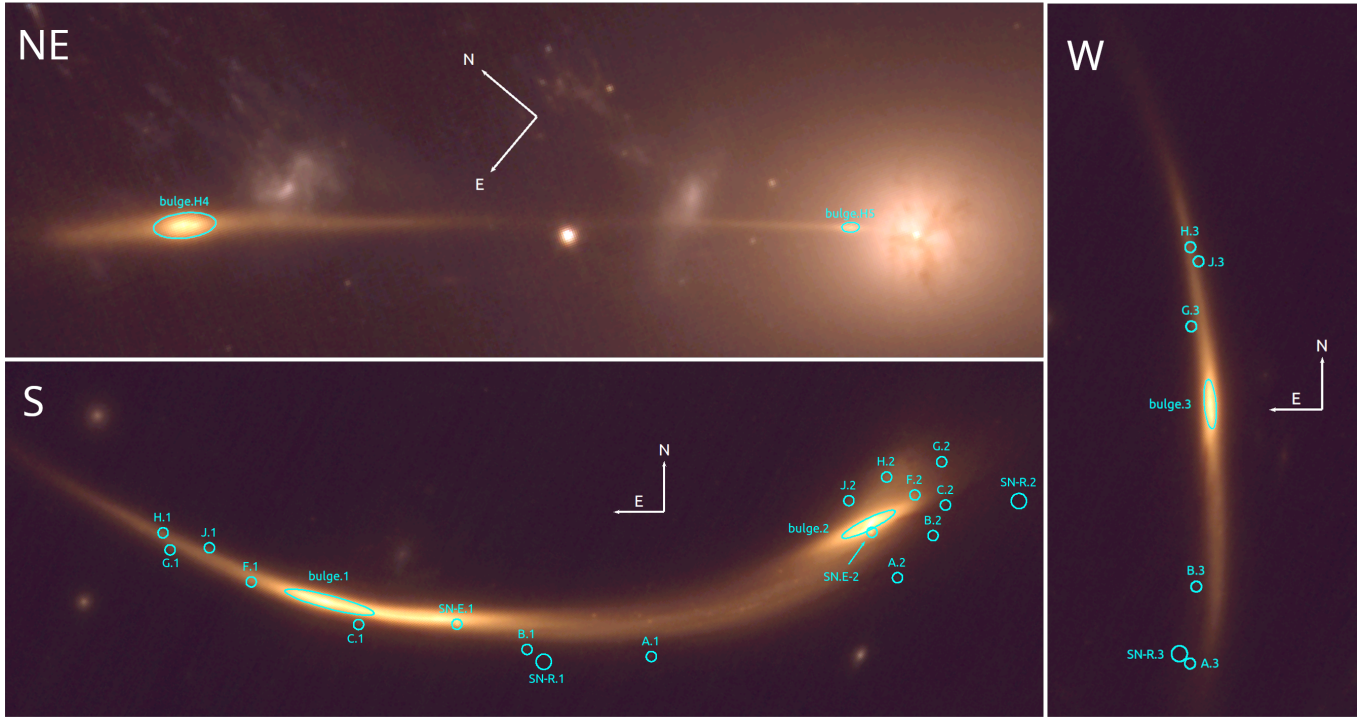


FIG. 3. **Lensing position constraints:** The positions of lensed features used to constrain the strong lens model, using the likelihood described in Section III B 2. The RGB color bands and scaling are the same as Figure 2. Three fields are shown here, showing lensed features of the quiescent source in the South, West, and North-East. In each field, a compass is displayed showing North and East; both segments of the compass are 1'' long for scale.

ponent are not used to constrain our mass model, and have no bearing on the primary results of this paper, we note that this gas component is clearly kinematically decoupled from the stellar component, and shows clear evidence of rotation about the galactic center (see Fig. 5). The stellar component shows negligible rotation, as expected in a BCG.

2. Systematics Test and Covariance

Measurements of stellar velocity dispersions can be highly sensitive to the wavelength range used, the choice of template library, and even the degree of the polynomial used to model background. As such, we conduct the following tests to verify the robustness of our kinematics map. Our approach follows Shajib *et al.* [59]. We aim to bracket a range of reasonable settings, all of which compute high-quality kinematics maps, and we compute a full kinematics map at each setting as described in the section above. We choose four different ‘axes’ along which we can reasonably change settings, and along each ‘axis’, we choose between 2 and 6 settings. These four axes, and their various settings, are:

- **Wavelength Range:** We extract and fit six different rest-frame wavelength ranges: 3700-4450Å, 3750-4500Å, 3800-4550Å, 3650-4550Å,

3700-4600Å, 3750-4650Å.

- **Background Polynomial Order:** The degree of the additive polynomial used to represent the background. We use three separate values, 4 through 6.
- **Input Template Library:** We use the XSL stellar template library as described in Section III C 1. As in Shajib *et al.* [59], we bisect the XSL library into two subsets, and compute kinematics maps with each subset. This results in three possible settings: ‘Full’ XSL library, bisected half-‘A’, and bisected half-‘B’.
- **Dust extinction:** The central galaxy of MACSJ0138 exhibits clear evidence of dust extinction, most evident in JWST NIRCcam imaging (c.f. Fig 3, NE field). We utilize two possible settings. The first ignores any effect of dust on the spectral fits. The second uses the one-parameter attenuation curve presented in Calzetti *et al.* [68], applying the same attenuation to both the stellar and gas components. The dust extinction is allowed to vary between 0 and 4 magnitudes, and is allowed a different value in each voronoi bin.

These constitute 108 possible settings, and produce 108 maps of the BCG’s stellar kinematics. For each of these measured kinematics maps, we draw 1000 random

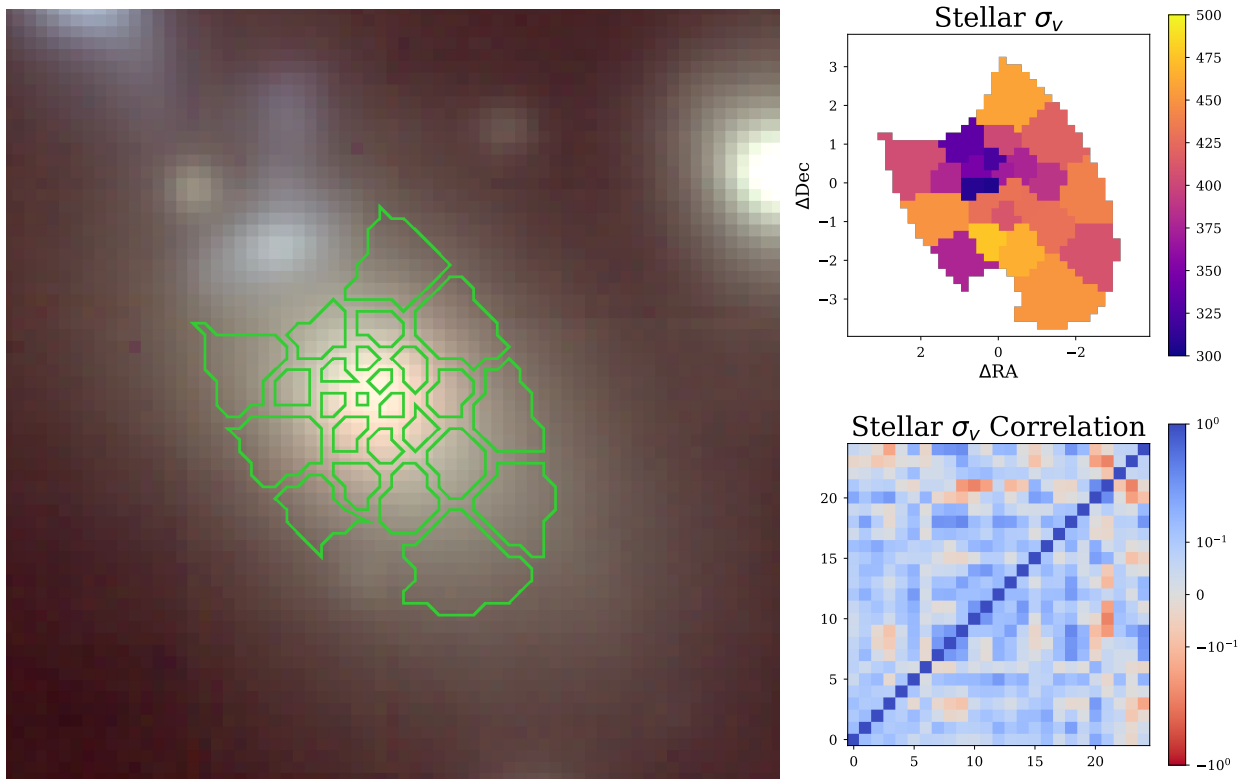


FIG. 4. The central galaxy of MACSJ0138, and the LOS stellar velocity dispersions measured in this work. **Left:** MUSE color imaging of the central galaxy, with the Voronoi bins used in this work overlaid in green. **Upper Right:** The LOS stellar velocity dispersion in each bin, in km/s. **Lower Right:** The correlation matrix of the LOS velocity dispersion in all 25 spatial bins, displayed in a `symlog` scaling with a linear threshold of 0.2.

realizations of the velocity dispersion map using the statistical errors produced by `ppxf`. From these 108,000 samples of the velocity dispersion in each voronoi bin, a mean and covariance are computed. The resulting best-fit kinematics map and correlation matrix are shown in Fig. 4. This covariance Σ is used in a conventional multivariate-Gaussian likelihood, as described in Section III C 4.

We find our resulting kinematics map to be consistent across all settings, with systematic uncertainty subdominant to statistical uncertainty in all but one spatial bin. Note that while Knabel *et al.* [61] have demonstrated the leading systematic uncertainty comes from the choice of template library, and advocate comparing a wide array of such libraries, they demonstrate this uncertainty is at most $\mathcal{O}(3\text{-}4\%)$ in fits to MUSE spectra. This is well below the $\approx 10\%$ uncertainty per bin measured in this work. See Appendix C for further discussion.

3. BCG Light Profile

The central galaxy’s light profile is represented as a Multi-Gaussian Expansion (MGE), measured using `MGEfit`[43] on the ACS/WFC F555W imaging. This band corresponds closely to the spectral wavelength

range used to measure stellar kinematics. We apply `MGEfit` in an ellipse aligned with and centered on the BCG, with a semi-major axis of $7''$ and a semi-minor axis of $5.5''$, excluding several regions contaminated by member galaxies and other LOS structure, as shown in Figure 6. Using an initial `ngauss` of 30, the resulting best-fit MGE contains 6 Gaussian components.

4. JAM Model and Likelihood

We compute the predicted stellar kinematics map using the widely used JAM package [44, 45, 69]. JAM requires two primary inputs, each represented as an MGE: (1) the luminous tracer used to measure the kinematics (in this case, the light profile of the central galaxy), and (2) the mass profile in which that tracer is embedded. The former is described in Section III C 3. For the latter, we combine the BCG stellar profile scaled by a mass-to-light ratio with the SIDM-modified dark matter density profile. The dark density profile is decomposed into an MGE via the `mge_fit_1d` function provided with `MGEfit`.

In addition, JAM requires several further parameters: a point spread function (PSF) model; the inclination angle relative to the line-of-sight; and the velocity anisotropy. The inclination angle, i , is also relevant to

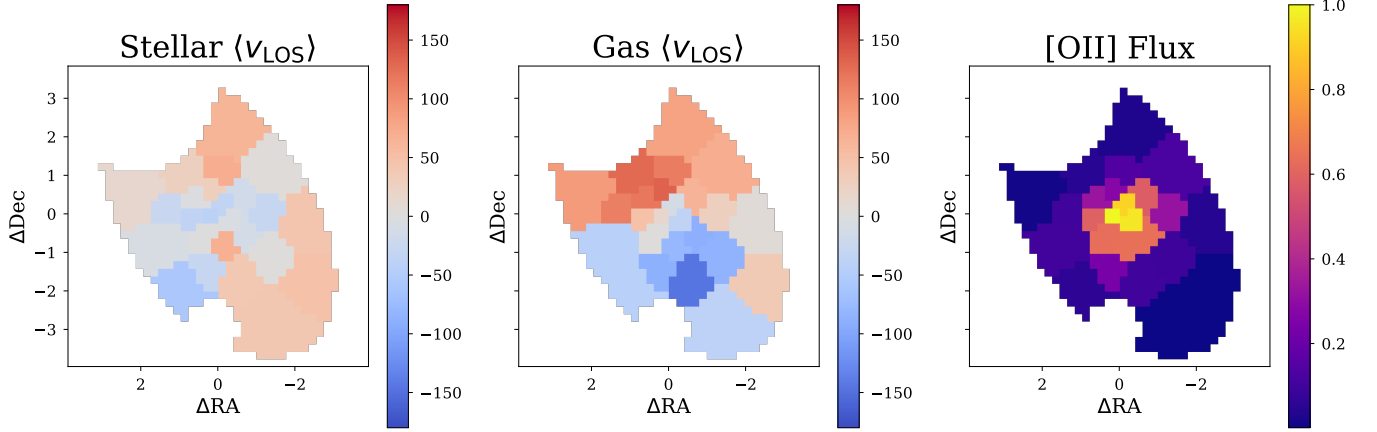


FIG. 5. Additional features of the central galaxy of MACSJ0138 measured with MUSE IFU spectra. Axes show offsets from the BCG center in arcseconds. **Left:** The measured LOS velocity of the stellar component in km/s, showing negligible rotation. In all Voronoi bins, $(\langle v \rangle / \sigma_v)^2 < 0.04$. **Center:** The measured LOS velocity of the emission lines in km/s, showing clear evidence of rotation. **Right:** Observed flux-per-spaxel of [O II] 3729Å, showing the spatial extent of gas emission. Flux is normalized by the brightest Voronoi bin.

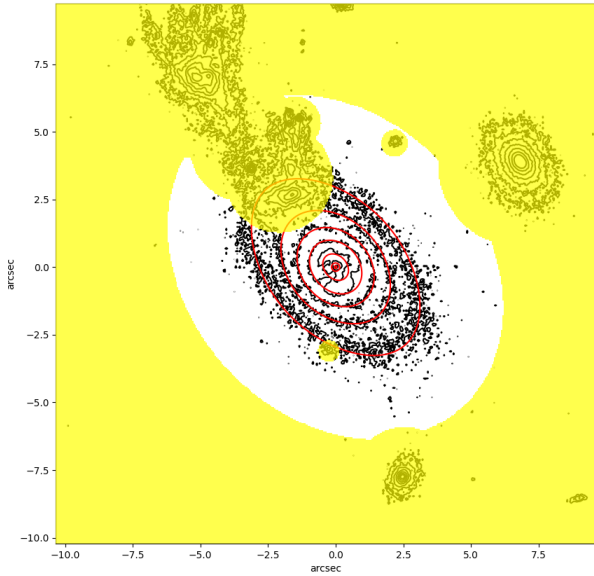


FIG. 6. The MGE approximation of the central galaxy's light profile, as provided by MGEfit. Regions in yellow are excluded from the fit. Black contours represent ACS F555W imaging data, and red contours represent the MGE profile. See Section III C 3 for details.

the triaxiality of the lensing halo, and has been described in Appendix B. The meaning of the velocity anisotropy β depends on whether the cylindrical [44] or spherical [69] alignment of the velocity ellipsoid is chosen, and whether the halo mass model is prolate or oblate. In this work, we use a spherical alignment of the velocity ellipsoid, where $\beta_{\text{sph}} = 1 - \sigma_\theta^2 / \sigma_r^2$, and $\beta_{\text{sph}} = 0$ indicates isotropic velocity of the stellar population. As noted in Birrer *et al.*

[62], JAM models with spherical and cylindrical alignment have been found to generally agree [69, 70], and both Shajib *et al.* [59], Birrer *et al.* [62] use the spherical alignment in joint models of lensing and dynamics. Considerable uncertainty, however, exists on the value of the velocity anisotropy β ; in this work, we adopt a flat prior on $\beta_{\text{sph}} \sim \mathcal{U}(-0.4, 0.4)$, slightly wider than the allowed values in [59, 62].

We use a simple Gaussian model of the PSF of our IFU data, from which the kinematics are measured. Metadata provided with the MUSE cube suggest the seeing varied between FWHM 0.66" and 0.8" over the course of the observations. In addition, we perform a simple test to compare our the relative seeing between the HST F555W imaging and the MUSE IFU data. Given the MGE model computed in Section III C 3, we convolve by a single-Gaussian PSF model to compute a predicted, PSF-smoothed image, and compare to the IFU cube summed between 5300 and 5700Å. Residuals between these suggest the true PSF at the MUSE slicer could be higher, up to around $\sim 1.15''$ FWHM. We thus assume a single-component Gaussian PSF, and adopt a prior on its size $\sigma_{\text{PSF}} \sim \mathcal{U}(0.35'', 0.5'')$, spanning FWHM values of approximately 0.5" to 1.2".

Given all the above inputs, for each spatial bin i , the predicted luminosity-weighted velocity dispersion is:

$$\langle \sigma_{\text{los},i}^2 \rangle = \frac{\int_{\Theta_i} I \langle v_{\text{los}}^2 \rangle \otimes \text{PSF} d^2\theta}{\int_{\Theta_i} I \otimes \text{PSF} d^2\theta} \quad (9)$$

Where Θ_i denotes the aperture of the i th spatial bin, $\otimes \text{PSF}$ denotes convolution by the PSF, and $\langle v_{\text{los}}^2 \rangle$ is the predicted LOS velocity dispersion at position θ computed by JAM. As in Shajib *et al.* [59], we take the first velocity moment to be negligible, leaving $\langle \sigma_{\text{los}}^2 \rangle = \langle v_{\text{los}}^2 \rangle$. (See also Figure 5.) With our measured kinematics map

$\sigma_{\text{los}}^{\text{obs}} = \{\sigma_{\text{los},i}^{\text{obs}}\}$ and covariance matrix Σ , the likelihood is therefore:

$$\Delta\sigma = \sigma_{\text{los}}^{\text{obs}} - \langle\sigma_{\text{los}}\rangle \quad (10)$$

$$\mathcal{L}(\sigma_{\text{los}}^{\text{obs}}|\mathcal{M}) = \frac{1}{\sqrt{(2\pi)^k|\Sigma|}} \exp\left(-\frac{1}{2}(\Delta\sigma)^T \Sigma^{-1}(\Delta\sigma)\right) \quad (11)$$

Where \mathcal{M} denotes our model parameters.

IV. RESULTS

Given the model, constraints, and likelihoods described in Section III, we compute three sets of posteriors. First, we present ‘lensing-only’ results, using only the strong lensing constraints; second, we present the ‘kinematics-only’ constraints, derived only from the measured kinematics map of the BCG; lastly, we present a joint model of the combined lensing and kinematics constraints.

All cosmology-dependent quantities use the best-fit parameters from Planck 2015 (P15) [71]. The following posteriors were obtained with the **emcee** ensemble MCMC sampler [72]. For the kinematics-only constraints, 80 walkers were used, whereas the lensing-only and joint results utilized 48 walkers each. While the kinematics-only result used a single sampler run, the lensing-only and joint posteriors were each estimated with two independent sampler runs in order to check the consistency of results. All samplers used a combination of ‘moves’, primarily the original **StretchMove** presented in Goodman and Weare [73], but with some additional weight given to **DEMove** and **DESnookerMove** [74, 75] to better explore multimodal posteriors.

All corner plots in this work were made with **corner** [76]. In all corner plots of posteriors, 2D contours shade the 1- and 2- σ posteriors, and 1D posteriors overlay the -1σ , median, and $+1\sigma$ confidence intervals with dotted vertical lines. The priors and posteriors of all parameters for all three models are shown in Table II.

A. Lensing-Only Results

The lensing-only model consists of seventeen parameters, constrained by 29 measured positions of 10 source features listed in Table I. As stated above, two independent **emcee** samplers of 48 walkers each were run for this model, in order to verify the robustness of posteriors. Both samplers ran for over 1,220,000 iterations, and yielded consistent estimates of the mean autocorrelation time of $\sim 52,450$ and $\sim 52,270$ iterations. This extremely long autocorrelation time suggests that **emcee** struggled to efficiently sample this parameter space, likely due to a complex likelihood surface. Nevertheless, we consider these results to be robust: the

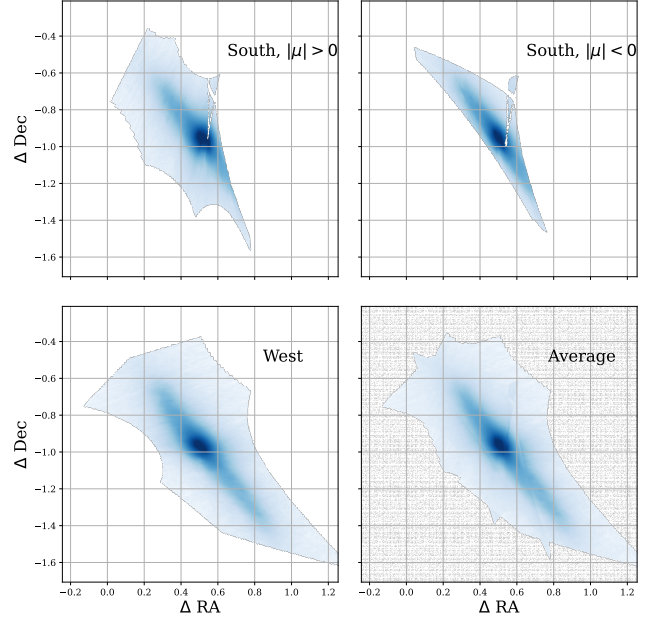


FIG. 7. **Lensing-Only Fit:** Source plane projection of the observed lensing arcs of the primary source at $z \approx 1.95$. **Top:** Luminosity of the southern arc, separated into the positive and negative magnification images. **Bottom Left:** The luminosity of the western arc. **Bottom Right:** The average of the former three images, demonstrating their consistency.

two independent samplers produced posteriors which are quantitatively and qualitatively consistent.

The predicted source-plane light derived from the southern and western arcs is shown in Figure 7, using the best fit mass model and NIRCам F150W imaging. The imaging was cropped to regions tightly bracketing the observed arcs, and the positions of each observed pixel were projected to the source plane given the best-fitting lens model. They were then interpolated to a grid of source-plane pixels with the **scipy** method **griddata**.

The lensing favors an overall DM halo with ellipticity closely aligned to the axis of the central galaxy, yielding $\phi = 44.3^{+1.8}_{-1.7}$ degrees East-of-North, compared to the BCG’s position angle of 42° . The position of the overall DM halo is also consistent with the center of the BCG, although the lensing alone favors a DM halo centered slightly to the south.

The lensing only model gives constraints on the mass-to-light ratio, mass, and concentration of $\log_{10} \Upsilon_* = 0.5^{+0.1}_{-0.2}$, $\log_{10}(M_{200\text{m}}/M_\odot) = 14.9 \pm 0.2$, $c_{200\text{m}} = 10^{+2}_{-3}$. The isothermal radius is constrained to be $\log_{10}(r_1/\text{kpc}) = 2.3^{+0.3}_{-0.9}$.

B. Kinematics-Only Results

The kinematics model has nine parameters (the seven shared parameters describing the BCG and cluster DM

Parameter	Description	Prior	Lensing Result	Kinematics Result	Joint Result
Shared Parameters					
$\log_{10} \Upsilon_*$	BCG stellar mass-to-light ratio	$\mathcal{N}(0.31, 0.3)$	$0.50^{+0.12}_{-0.21}$	$0.40^{+0.21}_{-0.29}$	$0.47^{+0.19}_{-0.35}$
$\log_{10}(\frac{M_{200m}}{M_\odot})$	Overall halo NFW mass	$\mathcal{U}(13.5, 15.5)$	$14.90^{+0.20}_{-0.17}$	$14.52^{+0.61}_{-0.59}$	$14.81^{+0.14}_{-0.12}$
c_{200m}	Overall halo NFW concentration	$\mathcal{U}(5, 15)$	$10.14^{+2.11}_{-3.03}$	$10.73^{+2.93}_{-3.41}$	$9.92^{+2.19}_{-1.88}$
$\log_{10}(r_1/\text{kpc})$	Isothermal Jeans radius, defines SIDM behavior	$\mathcal{U}(0.0, 3)$	$2.28^{+0.28}_{-0.92}$	$1.69^{+0.60}_{-0.95}$	$1.58^{+0.69}_{-0.99}$
q	3D halo prolate axis ratio	$\mathcal{U}(0.3, 1)$	$0.64^{+0.05}_{-0.10}$	$0.67^{+0.22}_{-0.24}$	$0.61^{+0.05}_{-0.13}$
$\cos(i)$	Halo inclination relative to LOS	$\mathcal{U}(0, 1)$	0.44 ± 0.29	$0.73^{+0.18}_{-0.40}$	$0.51^{+0.28}_{-0.32}$
ϕ	Position angle of projected ellipticity in the plane of the sky. East-of-North	$\mathcal{U}(-48^\circ, 132^\circ)$	$44.3^{+1.8}_{-1.7}$	$42.0^{+43.1}_{-43.3}$	$43.6^{+1.6}_{-1.5}$
Lensing Parameters					
x_{halo}	Horizontal offset between halo and BCG center, arcsec	$\mathcal{N}(0.0, 0.3)$	$-0.10^{+0.22}_{-0.26}$	—	$0.02^{+0.16}_{-0.18}$
y_{halo}	Vertical offset between halo and BCG center, arcsec	$\mathcal{N}(0.0, 0.3)$	$-0.33^{+0.23}_{-0.26}$	—	$-0.25^{+0.19}_{-0.21}$
γ_1	External shear component 1	$\mathcal{N}(0.0, 0.05)$	0.02 ± 0.01	—	0.02 ± 0.01
γ_2	External shear component 2	$\mathcal{N}(0.0, 0.05)$	$-0.08^{+0.03}_{-0.02}$	—	-0.06 ± 0.02
α	Slope of the Faber-Jackson relation	$\mathcal{N}(0.26, 0.06)$	0.26 ± 0.06	—	0.26 ± 0.06
$\sigma_{\text{LT}}^{\text{piv}}$	dPIE velocity dispersion scale of Faber-Jackson relation, km/s	$\mathcal{N}(199.1, 22.3)$	$184.8^{+19.3}_{-20.4}$	—	$188.8^{+19.4}_{-19.5}$
$\sigma_{\text{LT}}^{\text{J1}}$	dPIE velocity dispersion of J1, km/s	$\mathcal{N}(100, 50)$	$66.5^{+31.0}_{-33.0}$	—	$65.1^{+35.7}_{-33.7}$
$\sigma_{\text{LT}}^{\text{J3}}$	dPIE velocity dispersion of J3, km/s	$\mathcal{N}(100, 50)$	$51.0^{+24.9}_{-27.0}$	—	$49.6^{+25.3}_{-26.8}$
r_s^{J4}	dPIE velocity dispersion of J4, km/s	$\mathcal{N}(100, 50)$	19.6 ± 5.2	—	$19.5^{+5.1}_{-5.2}$
$\sigma_{\text{LT}}^{\text{J4}}$	dPIE scale radius of J4, kpc	$\mathcal{N}(20, 5)$	$48.3^{+14.7}_{-16.8}$	—	$56.6^{+12.0}_{-14.6}$
Kinematics Parameters					
β_{sph}	Velocity anisotropy	$\mathcal{U}(-0.4, 0.4)$	—	$-0.09^{+0.21}_{-0.19}$	$-0.15^{+0.15}_{-0.14}$
σ_{PSF}	Gaussian PSF size, arcsec	$\mathcal{U}(-0.35, 0.5)$	—	0.43 ± 0.05	0.43 ± 0.05
Derived Parameters					
σ/m	SIDM Cross Section, cm^2/g	—	$0.16^{+0.50}_{-0.15}$	$0.04^{+0.35}_{-0.03}$	$0.02^{+0.18}_{-0.02}$
$\log_{10}(\sigma/m)$	Logarithm of σ/m in cm^2/g	—	$-0.8^{+0.6}_{-1.1}$	$-1.4^{+1.0}_{-0.8}$	$-1.7^{+1.0}_{-0.8}$
σ_0	Thermal velocity of isothermal region, km/s	—	919^{+88}_{-333}	565^{+375}_{-250}	691^{+200}_{-406}
V_{max}	Maximum circular velocity of cluster DM halo	—	1518^{+161}_{-137}	1144^{+640}_{-410}	1422^{+95}_{-82}
q_{2D}	Projected apparent axis ratio of cluster DM	—	0.68 ± 0.03	$0.82^{+0.14}_{-0.28}$	0.67 ± 0.02
$\log_{10} M_{20}^{\text{enc}}$	Enclosed mass within 20kpc	—	$12.22^{+0.14}_{-0.16}$	$12.24^{+0.13}_{-0.19}$	$12.34^{+0.04}_{-0.05}$
$\log_{10} M_{100}^{\text{proj}}$	Projected mass within 100kpc	—	13.79 ± 0.03	$13.61^{+0.29}_{-0.33}$	$13.78^{+0.02}_{-0.04}$

TABLE II. **Results:** Priors and posteriors for all three models fit in this work. In the priors column, $\mathcal{U}(a, b)$ denotes a uniform prior on the interval $[a, b]$, and $\mathcal{N}(\mu, \sigma)$ denotes a Gaussian prior of mean μ and variance σ^2 . The ‘Result’ columns list the median and 1σ bounds on each parameter. The shared, lensing-only, and kinematics-only parameters and priors are explained in detail in Sections III A, III B, and III C respectively; for convenience, brief descriptions of each parameter are included here.

halo, and β_{sph} and σ_{PSF}), and is constrained by the measured velocity dispersion in 25 Voronoi bins. The 80-walker **emcee** chain for this model ran for 192,648 iterations, with a mean autocorrelation time of 910 iterations across all nine parameters. Having run for over 200 autocorrelation times, we consider these samples to be exceedingly stable and well converged.

This model provides constraints of $\log_{10} \Upsilon_* = 0.4^{+0.2}_{-0.3}$, $\log_{10}(M_{200m}/M_\odot) = 14.5 \pm 0.6$, $c_{200m} = 11 \pm 3$, and $\log_{10}(r_1/\text{kpc}) = 1.7^{+0.6}_{-1.0}$. These are fully consistent with the lensing-only model.

The predicted kinematics map of the maximum likelihood sample is shown in Figure 8. The best-fit model yields a reduced χ^2 of 2.76. As expected, the stellar kinematics is most sensitive to the total mass within $\sim 20\text{kpc}$, and has only weak constraining power on the mass and concentration of the overall halo. It is reassuring, however, that the kinematics model alone yields parameters that are highly consistent with the lensing-only model: the posteriors on Υ_* are similar, and in M_{200m} - c_{200m} space, the 1σ posteriors of the lensing-only model lie almost entirely within those of the kinematics-only model.

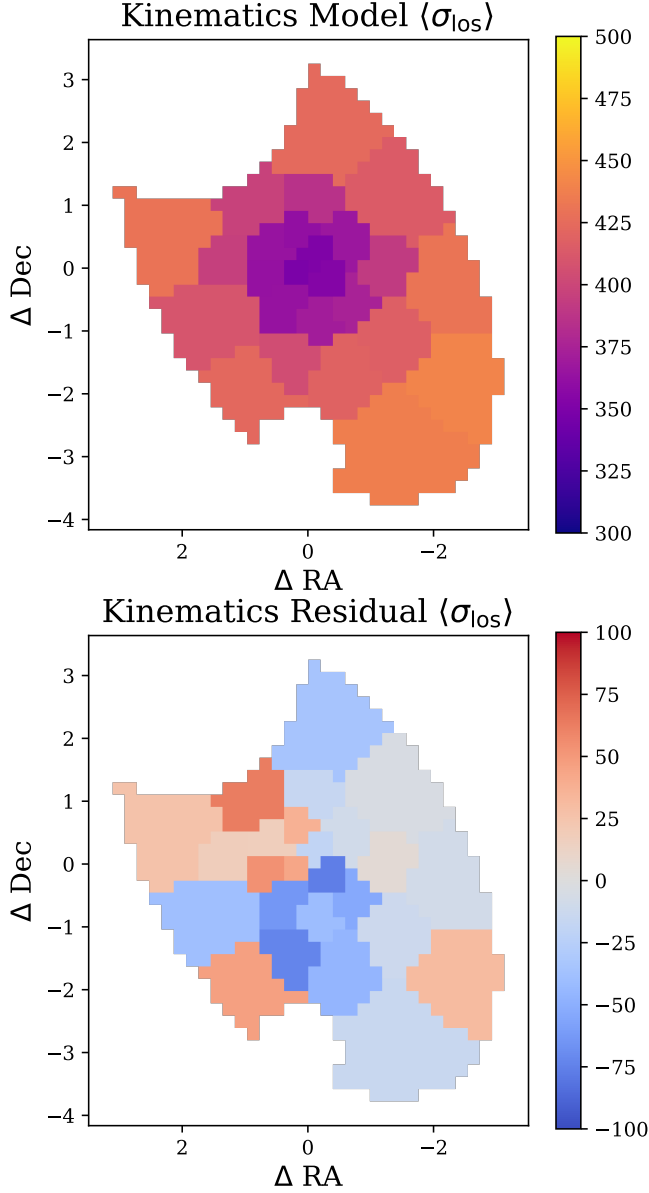


FIG. 8. **Kinematics Fit:** The best-fit predicted kinematics map and residual (predicted - data). Axes units are arcsec relative to BCG center, color map units are km/s.

A larger difference can be seen in the SIDM cross section σ/m , where the lensing alone prefers markedly higher values. Nevertheless, they are consistent, justifying a combination of both lensing and kinematics constraints.

Our kinematics model prefers an anisotropy $\beta_{\text{sph}} < 0$, implying $\sigma_{\theta}/\sigma_r > 1$. This preference only strengthens when lensing constraints are included, see Table II. Shajib *et al.* [63] similarly found $\sigma_{\theta}/\sigma_r > 1$ in both ground- and space-based IFU measurements of a galaxy-scale lens. While the PSF size σ_{PSF} is entirely unconstrained, it fortunately demonstrates almost no degeneracy with any other parameters.

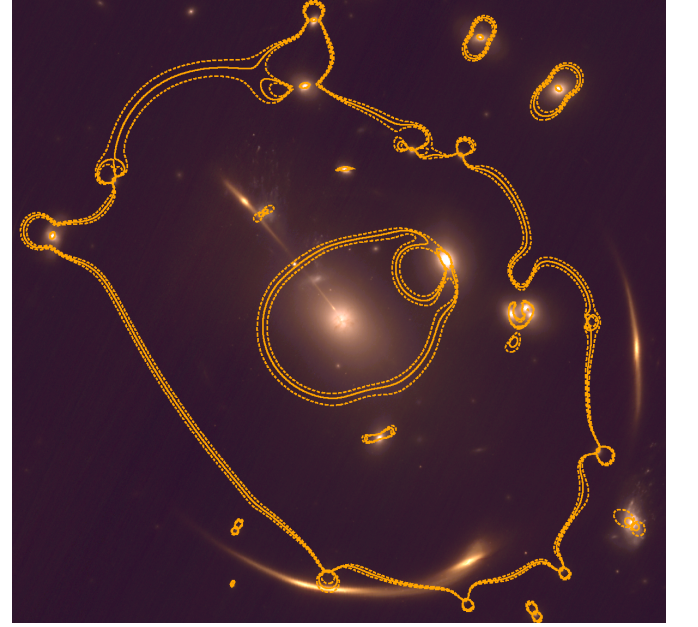


FIG. 9. **Critical Curves:** Posteriors on the lensing critical curves of the joint model. Median critical curves are displayed as a solid line, $\pm 1\sigma$ critical curves are dashed lines. Color bands and scaling are identical to Figure 2.

C. Combined Strong Lensing and Kinematics Results

The results of the joint model, combining strong lensing and stellar kinematics, are the primary result of this work. As in Section IV A, we run two separate *emcee* samplers of 48 walkers each to verify the robustness of these results. Reassuringly, *emcee* was able to sample the joint model more efficiently than the lensing-only model, despite having slightly higher dimensionality and a more expensive likelihood. This suggests the kinematics constraints contribute to a ‘smoothing-out’ of the likelihood surface. The two joint samplers both ran for over 660,000 iterations, yielding a mean autocorrelation time across all parameters of $\sim 21,400$ and $\sim 22,900$ iterations, substantially shorter than for the lensing-only model. Both independent sampling runs yielded nearly identical posteriors, and we consider these posteriors to be robust.

The predicted critical curves (positions of infinite magnification) from this model are displayed in Figure 9. To create this plot, the magnification field $\mu(\vec{\theta})$ was computed from 10,000 randomly drawn samples of the posterior. The median ($\pm 1\sigma$) critical curves are the contours where the median (15.9%, 84.1% quantile) of μ^{-1} is zero. As expected, the tangential critical curve divides the southern arc neatly into two images of positive and negative magnification, and the radial critical curve divides the central and North-East images near a point where their light is dimmest. These curves are very consistent with those derived from the lensing-only model, which is not overlaid to improve the clarity of

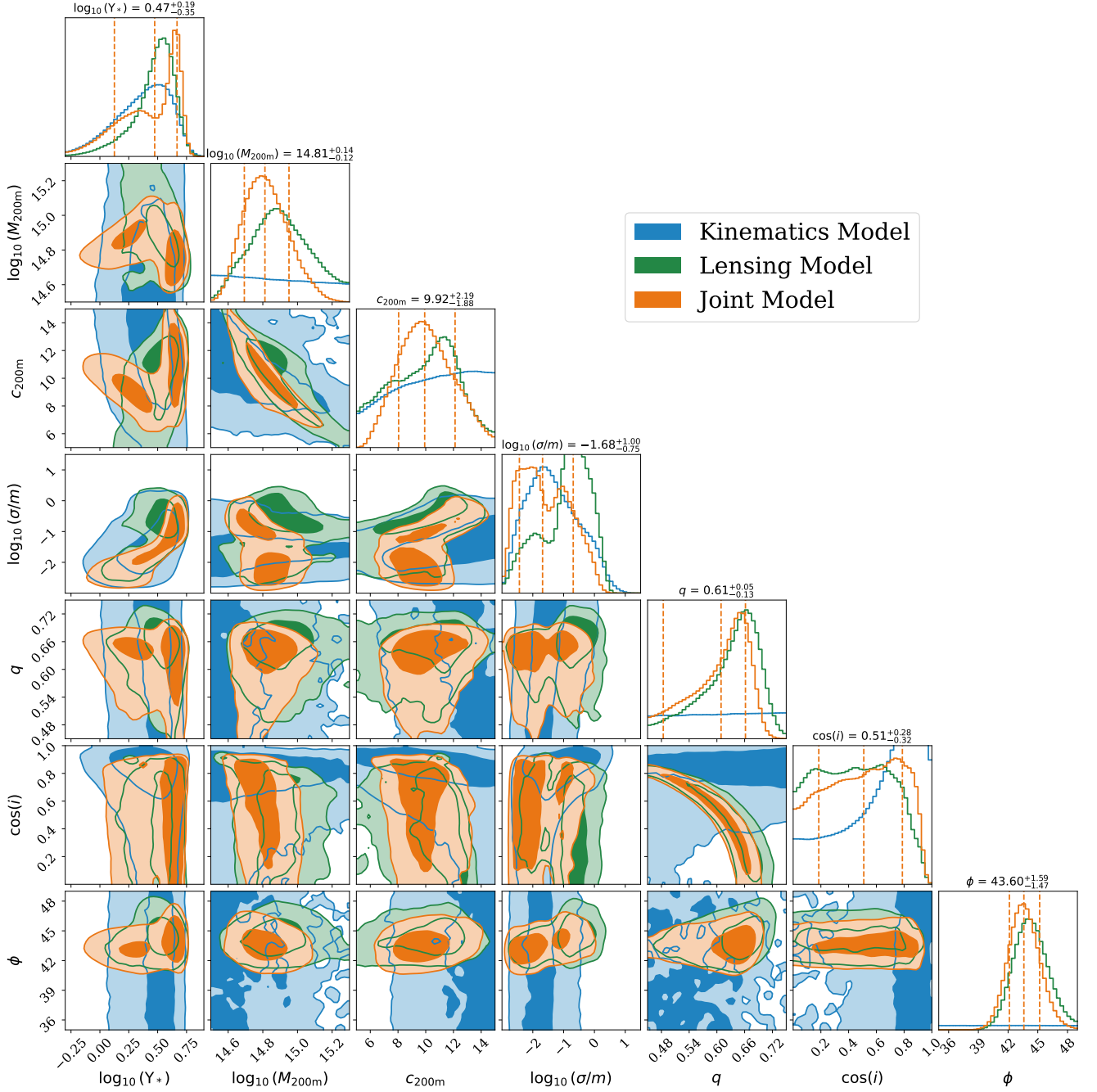


FIG. 10. Posteriors of shared parameters across all models. For every pair of parameters, colored contours show the 1- and 2- σ posteriors. At the top of each column, the median and $\pm 1\sigma$ posteriors are listed for the joint model, and marked with dashed vertical lines.

the plot. The predicted magnification at the conjugate points, however, differs between the joint and lensing-only models; see Section IV E for further discussion. The best-fit kinematics map from this joint model is nearly identical to that of the kinematics-only model, with a (non-reduced) χ^2 of 45.5, compared to 44.3 for the kinematics model shown in Figure 8.

This joint model yields constraints of $\log_{10} \Upsilon_* =$

$0.5^{+0.2}_{-0.4}$, $\log_{10}(M_{200m}/M_\odot) = 14.8 \pm 0.1$, $c_{200m} = 10 \pm 2$, and $\log_{10}(r_1/\text{kpc}) = 1.6^{+0.7}_{-1.0}$. For numerical constraints on other parameters, see Table II. Curiously, the joint posteriors exhibit a strong bimodality absent from either the kinematics- or lensing-only models. This is most evident in the Υ_* - M_{200m} space, see Fig. 10. In addition, the stellar mass-to-light ratio Υ_* is strongly degenerate with the SIDM cross section σ/m , with higher cross sections

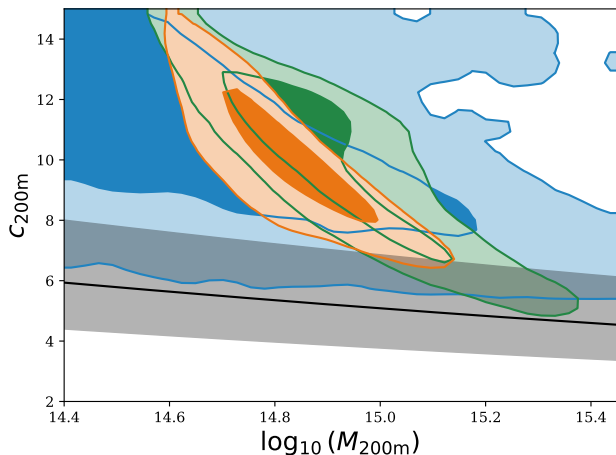


FIG. 11. **Mass-Concentration:** A comparison of the posteriors on M_{200m} and c_{200m} in this work to theoretical predictions. The mass-concentration relation of L16 is displayed in black, with a shaded band showing 0.13 dex scatter. The L16 relation was computed at the cluster redshift, and translated to M_{200m}, c_{200m} using Colossus [77].

occurring exclusively at high Υ_* .

While the kinematics and lensing models alone both prefer a cluster halo with relatively high concentration, the significance of this preference increases in the joint model. The posteriors of all models are reproduced in Figure 11, and compared to the expected concentration from Ludlow *et al.* [78] (L16) with a scatter of 0.13 dex. These choices are identical that used in Robertson *et al.* [47]. The joint model prefers a halo concentration around $\sim 2\sigma$ higher than the L16 relation.

D. External Shear

The lensing-only and joint models above yielded external shear with magnitude $|\gamma_{\text{ext}}|$ of 0.09 ± 0.02 and 0.07 ± 0.01 , respectively. The external shear term is intended to represent the contribution of cosmic shear sourced by large scale structure, and other mass near the line of sight, which are fundamental systematic uncertainties in strong gravitational lensing. While the motivation of this approach is to generically capture and account for any such perturbations, Etherington *et al.* [79] has demonstrated in galaxy-galaxy lenses that the magnitude and direction of SL-derived γ_{ext} shows little correlation with known weak lensing shear, and is instead highly correlated with the elliptical orientation of the lens itself. They suggest that, in practice, the external shear accounts for structure of the lens mass which parametric models fail to properly describe.

To investigate whether the measured γ_{ext} may be explained physically, we conduct the following test. In the MACSJ0138 field, there is a luminous red galaxy $\sim 2.5'$ to the south, which is likely associated with the

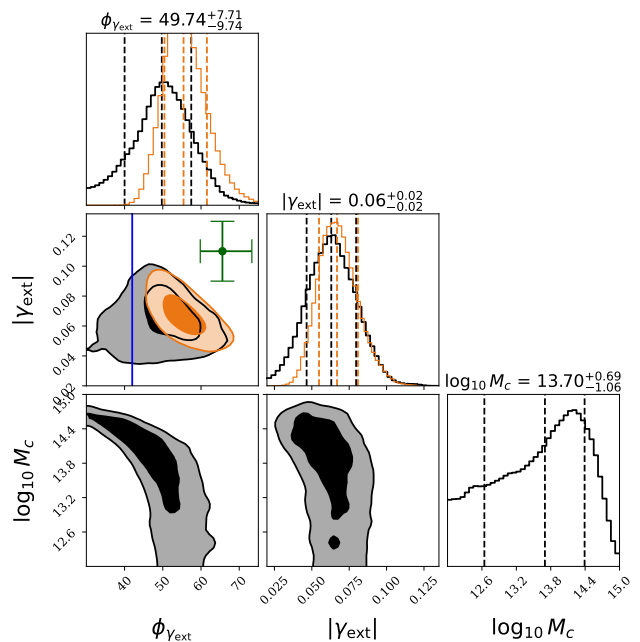


FIG. 12. **External Shear:** The direction and magnitude of the external shear γ_{ext} . Black contours show the results of the test described in Section IV D, and orange contours denote the results of the joint model. In $\phi_{\text{ext}} - |\gamma_{\text{ext}}|$ space, a blue line marks the orientation of the central galaxy of MACSJ0138, and a green point marks the result of [35].

MACSJ0138 cluster and may host a significant DM halo of its own. We conduct another *emcee* sampling of the joint likelihood, including a further NFW halo of fixed $c_{200m} = 6$ and varied $M_{200m} = M_c$ at the position of this bright LRG, (RA, Dec) = (01:38:06, -21:57:51). To simplify the parameter space, we identify six parameters with negligible degeneracy, and fix them to the median values obtained by the joint sampling in Section IV C. These parameters are $\alpha, r_s^{J4}, \sigma_{\text{LT}}^{J1, J3, J4}, \sigma_{\text{PSF}}$.

The results of this test are illustrated in Figure 12, showing posteriors on the position angle and magnitude of γ_{ext} , as well as the mass of the nearby NFW halo, M_c . Acebron *et al.* [35] also modeled MACSJ0138 with an external shear, and their measured γ_{ext} is overlaid for comparison. Allowing for the nearby mass slightly decreases the derived shear magnitude, suggesting this mass can only partly explain the observed shear. The data clearly prefer a substantial mass at the location of the LRG, with a mass up to $\sim 10^{14.4} M_\odot$. While the effect on the shear magnitude $|\gamma_{\text{ext}}|$ is slight, the nearby mass has a significant effect on the position angle of the shear, extending the posteriors to include the orientation of the central galaxy of MACSJ0138. Similarly, Etherington *et al.* [79] found that γ_{ext} frequently aligned with the lens orientation. Our lensing constraints additionally show a clear preference for the presence of this other mass: this test yielded a minimum lensing χ^2 of 3.5, significantly lower than the best lensing χ^2 of 4.08 produced

Feature Group	Requiem (2)		Encore (1)	
	Delay (d)	Median	Delay (d)	Median
a	55 ± 6	Jun 2016	41 ± 4	Sept 2023
b	0	Apr 2016	0	July 2023
c	-31 ± 5	Mar 2016	-300^{+31}_{-34}	Sept 2022
d	4245^{+343}_{-322}	Nov 2027	3507^{+291}_{-280}	Feb 2033
e	4372^{+339}_{-323}	Apr 2028	3819^{+307}_{-283}	Jan 2034

TABLE III. **Time Delays:** The predicted time delays between all five images of both lensed SNe, given in days. Delays are normalized relative to the southernmost image (b). The ‘Median’ columns give the median date of predicted peak SN brightness, rounded to the month. Image groups (d) and (e) are anticipated in the next decade; their dates are shown in bold.

by the fiducial joint model. Nevertheless, the presence of the extra mass results in little change to our parameters of interest compared to the joint model; the posteriors on Υ_* , $M_{200\text{m}}$, $c_{200\text{m}}$, and σ/m are all consistent within 1σ .

E. Supernovae Requiem and Encore

Here we present model-predicted time delays and magnifications of both lensed SNe. The predicted magnifications of previously observed SNe images are shown in Figure 13. For clarity, we use the same labels as Ertl *et al.* [34], Acebron *et al.* [35], and mark images which are not used as model constraints with an asterisk (*). In this nomenclature, images (2a, 2b, 2c) and (1a, 1b) correspond respectively to (SN-R.2, SN-R.1, SN-R.3) and (SN-E.2, SN-E.1) in our Table I. We additionally include predicted images (d*) and (e*), with predicted positions in the central and North-East radial arcs where neither supernova has yet been observed. While the lensing-only model provides very poor constraints on the magnifications, our joint model including kinematics yields clear predictions.

Time delays predicted by the joint model are listed in Table III. These are computed using the fixed P15 cosmology, with $H_0 = 67.7 \text{ km s}^{-1} \text{ Mpc}^{-1}$ and a time-delay distance $D_{\Delta t}$ of $\sim 1860 \text{ Mpc}$ for this lens and source. As in Rodney *et al.* [27], time delays are normalized relative to the southernmost image of both SNe, labeled (b) here. Dates of peak brightness are estimated from the observed SN ages reported by Rodney *et al.* [27] and Dhawan *et al.* [31] for Requiem and Encore, respectively. These results imply the next observed image will be feature (d) of SN Requiem in late 2027 with ~ 1 year uncertainty, approximately two years from the date of this publication.

V. DISCUSSION

We have presented independent and joint constraints from strong lensing and stellar kinematics models. The

constraints on parameters of interest (chiefly the stellar mass-to-light ratio Υ_* , halo mass and concentration, and SIDM cross-section) are remarkably consistent between the individual probes. The joint model provides notably tighter constraints on the mass and concentration, and a more stringent upper limit on the SIDM interaction cross-section. As a means of comparison between all three models in this work, the enclosed 3D mass relation $M(< r)$ for the DM, BCG stellar, and total mass are displayed in Figure 14.

Our results exhibit a strong bimodality in the stellar mass-to-light ratio Υ_* , and less so in the SIDM cross section. These modes correspond to a strong degeneracy between Υ_* and σ/m . This degeneracy is not unexpected: a high stellar mass atop a cored DM density may resemble a low stellar mass in a cuspy DM density profile. Therefore, our method’s ability to distinguish baryonic and dark mass is limited. Better knowledge of Υ_* in central cluster galaxies may therefore help constrain the inner DM slope.

In this work, the lensing and kinematics data vectors provided similar data degrees of freedom (d.o.f.), at 25 and 38 respectively. Pixel-level modeling of strong lensing features, by contrast, typically uses data vectors of hundreds of points or more. Wang *et al.* [65], which also studied a strong lensing cluster, notes this as a potential difficulty in combining strong lensing and kinematics measurements. Combining lensing data with hundreds of data d.o.f., with kinematics likelihoods of typically a few dozen d.o.f., can therefore yield minimal change over a lensing-only model, as the χ^2 of the lensing data will typically dwarf the χ^2 of the much smaller kinematics data vector. Wang *et al.* [65] therefore do not combine stellar kinematics with pixel-level image modeling, and only present joint posteriors for a conjugate point likelihood with kinematics, similar to what was done here. Pixel-level SL modeling is beyond the scope of the present work, but we note this as a consideration for future work combining kinematics and strong lensing.

As an additional test, we sampled a variation on our model which explicitly represented the mass of a nearby bright galaxy in Section IV D. While this choice yielded minimal change to our key parameters (chiefly Υ_* , $M_{200\text{m}}$, $c_{200\text{m}}$, and σ/m), implying our results are robust, our likelihood nonetheless strongly preferred the presence of another halo. Future precision models of MACSJ0138 may benefit from explicitly including this halo.

A. Consistency with Other Mass Models

Early work modeling the strong lensing in MACSJ0138 included Newman *et al.* [32] and Rodney *et al.* [27], which presented the discovery of SN Requiem. More recent models include Ertl *et al.* [34], Acebron *et al.* [35], which leverage deep JWST and MUSE data and include SN Encore. Below we compare our results with these previ-

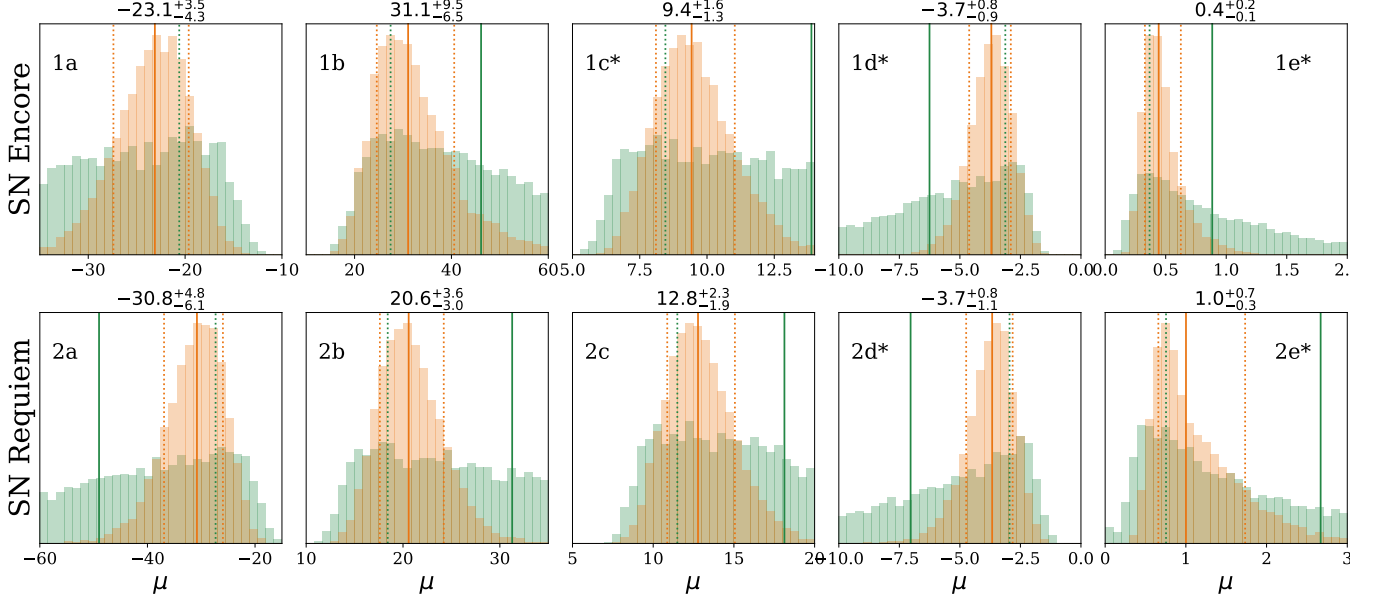


FIG. 13. **Model SNe Magnifications:** The magnification of the observed and predicted images of SNe Requiem and Encore. Each histogram is generated from 10,000 randomly chosen samples of the `emcee` chains. The posteriors of the lensing-only and joint model are shown in green and orange respectively, and their median (1σ) limits are overlaid as solid (dotted) vertical lines. The title of each subplot lists the result of the joint model. Images which are not used to constrain the model are marked with an asterisk (*), including image groups (d*) and (e*) which have not been observed.

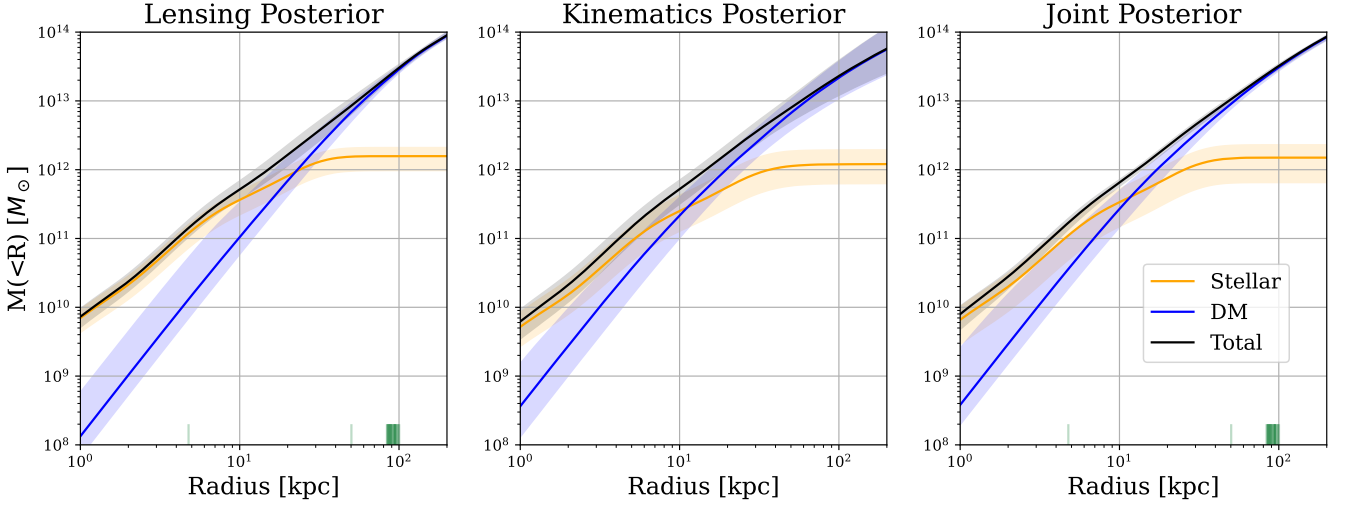


FIG. 14. **Enclosed Mass:** Posteriors on the enclosed 3D mass for all three models presented here. At the bottom of each plot, a shaded blue region represents the radii constrained by stellar kinematics, and vertical green lines represent the projected radii of strong lensing constraints.

ous models. While our results strongly disagree with the model presented in [27], they appear broadly consistent with the newest mass models [34, 35].

Common diagnostics used in cluster-scale strong lensing include the critical curves (the contours of infinite magnification), and the root-mean-square scatter between predicted and observed images, commonly called

the RMS. The critical curves predicted by our joint model were presented above in Figure 9. While the critical curves can only enable a qualitative comparison, we note that ours appear very consistent with the newest mass models, see Fig. 1 of [35] and Fig. 8 of [34]. Additionally, we present the image-plane RMS of all features used to constrain our model in Table IV. We caution against

Feature	Lensing Best-Fit	Lensing Posterior	Joint Best-Fit	Joint Posterior
SN-E	0.12	$0.11^{+0.08}_{-0.07}$	0.09	$0.11^{+0.07}_{-0.06}$
SN-R	0.12	$0.14^{+0.13}_{-0.07}$	0.05	$0.12^{+0.10}_{-0.06}$
A	0.20	$0.21^{+0.16}_{-0.10}$	0.24	$0.21^{+0.14}_{-0.10}$
B	0.17	$0.17^{+0.15}_{-0.09}$	0.17	$0.17^{+0.13}_{-0.09}$
C	0.01	$0.05^{+0.03}_{-0.02}$	0.03	$0.05^{+0.03}_{-0.02}$
F	0.04	$0.06^{+0.04}_{-0.03}$	0.06	$0.05^{+0.04}_{-0.03}$
G	0.08	$0.11^{+0.07}_{-0.04}$	0.08	$0.10^{+0.05}_{-0.04}$
H	0.08	$0.10^{+0.07}_{-0.04}$	0.05	$0.09^{+0.05}_{-0.03}$
J	0.06	$0.09^{+0.07}_{-0.04}$	0.03	$0.08^{+0.05}_{-0.03}$
bulge	0.10	$0.20^{+0.10}_{-0.07}$	0.08	$0.20^{+0.10}_{-0.06}$
all	0.11	$0.16^{+0.06}_{-0.04}$	0.11	$0.16^{+0.05}_{-0.03}$

TABLE IV. **Image-plane RMS:** The RMS distance between observed and predicted positions of each feature group. The last row gives the combined RMS for all features. All entries are in arcseconds. The ‘Best-Fit’ columns give the result of the maximum likelihood sample.

direct comparisons of RMS between our work and other mass models, as we use an entirely different set of position constraints and sample a different likelihood. Nevertheless, both our lensing-only and joint models yield a small, best-fit RMS of 0.11 arcsec.

Reliable estimates of the lensing magnification are essential to any study of lensed sources, such as [33], and for accurate photometric classification of the observed SNe [27]. Our joint model magnifications are in clear agreement with the two most recent models [34, 35], with the magnifications of all observed sources within the 1σ errors of those in [35], and slightly below the absolute magnifications predicted by [34]. See Fig. 6 of [35] and Table 9 of [34] for comparison. The absolute magnifications $|\mu|$ for predicted images 1d* and 1e* of SN Encore are nearly identical to [35] as well ⁶. Compared to [34], we predict $|\mu|$ approximately 20% lower for the observed image groups (a,b,c). Our predictions for (d,e) are more discrepant, where our predictions are 60% higher and ~ 2 -5x lower respectively.

Our results, however, disagree significantly with the earlier model in Rodney *et al.* [27], which gave $|\mu|$ of observed images roughly 3-5x lower than ours. Acebron *et al.* [35] similarly noted that their predicted magnifications strongly disagree with previously reported lens models in [27, 32]. We do not consider this problematic, as we believe our mass model to be higher quality than that in [27], which predicted an unreasonably large ellipticity for the overall halo and a BCG more massive than the overall halo. Intriguingly, our results in this work also imply a very different time-delay baseline from [27],

which predicted a roughly 20-year delay between the observed images of SN Requiem and the next predicted image, placing the recurrence in the mid-2030s. Our model yields a much lower delay of roughly ~ 12 years, in which case SN Requiem would be seen again in the next few years, likely before 2030 (see Table III). Unfortunately, we are unable to compare these predictions to the newer models in [34, 35], which did not report forecasted time delays.

We stress that our group has independently measured the Faber-Jackson relation of the members of MACSJ0138 [29], chosen cluster members to include in the SL mass model, identified multiply imaged features to use as constraints, and uses an entirely different modeling code and parametrized mass model from other work on MACSJ0138. While agreement between our predicted magnifications and those in [34, 35] does not exclude systematic effects distorting the true magnifications, it is encouraging that these models agree with ours despite substantial differences in approach. Acebron *et al.* [35] suggests that the discrepancy between their reported magnifications and earlier work could be partly explained by the inclusion of newly identified sources at different redshift. However, this is unlikely to be true, as our model agrees with theirs despite not using the newly discovered sources. Lens modeling choices still have a large effect on predicted magnifications near the critical curves: our model agrees more closely with Acebron *et al.* [35] (which similarly used one cluster halo and an external shear) than it does with Ertl *et al.* [34] (which used two halos to describe the cluster DM, and no external shear).

VI. CONCLUSIONS

We have presented a detailed mass model of MACSJ0138, combining strong gravitational lensing and stellar kinematics measurements. With the aim of refining previous SIDM constraints on cluster scales, we have improved on the methodology of previous studies [14, 15]. From our combined model, we report a 95% CL upper limit on the SIDM cross section of $\sigma/m < 0.613 \text{ cm}^2/\text{g}$, at an interaction velocity $\langle v_{\text{pair}} \rangle < 2090 \text{ km/s}$. Though in this work, we studied a single system, we aim to apply this methodology to a sample of systems in the future. Further, these results and methods are of significant interest beyond SIDM. Effectively combining strong lensing and stellar kinematics is widely acknowledged as key to advancing the state-of-the-art of SL modeling. The inclusion of kinematic measurements has the potential to break the well-known mass sheet degeneracy, improving SL-derived cosmological constraints, particularly for time delay cosmography. The MACSJ0138 system is of intense interest, as the first known SL system to host multiple strongly lensed SNe; these results inform future constraints on the Hubble constant from this system.

Our combined kinematics and lensing model places considerably tighter constraints on SIDM interactions

⁶ Curiously, [35] lists the demagnified central image 1e* as having opposite sign, with a negative magnification. We consider this to likely be a mistake, demagnified central images always have positive parity.

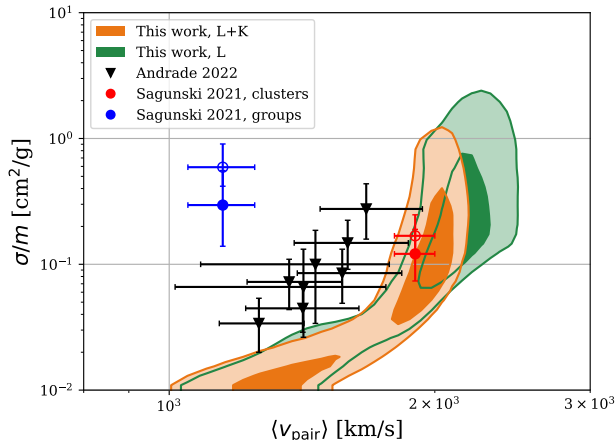


FIG. 15. **SIDM Interaction:** Constraints on the magnitude and velocity scale of SIDM interactions, compared to previous work. Black triangles show the eight clusters studied in [15], while the blue and red points show the full constraints from eight groups and seven clusters in [14]. Compare to Figure 3 of [14].

than either measurement alone. Our posteriors on the magnitude and velocity scale of self-interaction are shown in in Figure 15, with results from [14, 15] overlaid for comparison. For a detailed list of posteriors on measured parameters, along with derived quantities of interest, the reader is referred to Table II. The lensing results alone exhibit a bimodality in σ/m , with a marked preference for the higher mode near $\sigma/m = 1 \text{ cm}^2/\text{g}$. The inclusion of kinematics constraints suppresses this mode. Notably, our joint results still exhibit a clear bimodality, with one mode at high values of Υ_* , σ/m , and $\langle v_{\text{pair}} \rangle$, and one at lower values of those three parameters. This degeneracy resembles that of the aggregate sample of clusters in Andrade *et al.* [15], though offset in $\langle v_{\text{pair}} \rangle - \sigma/m$ space. Improved knowledge of the true stellar mass-to-light ratio of BCGs could therefore break this degeneracy, providing tighter constraints on the inner dark matter halo.

Extending the methodology in this work to a sample of clusters would greatly improve constraints on SIDM. However, challenges remain. The selection effects inherent in such a sample remain a concern, as strong lensing halos are preferentially concentrated and elongated along the line-of-sight. Fortunately, other probes of the cluster density profile exist with very different systematics, such as X-ray observations of the hot intracluster medium (ICM) and weak lensing measurements. The density profile inferred from X-ray observations of the ICM could be particularly powerful for SIDM studies, as it constrains the cluster halo at similar radii as SL. Weak lensing alone is unlikely to provide meaningful constraints on SIDM [25], but is highly useful in combination with the other probes here to ensure the inferred cluster mass is accurate on larger scales.

We additionally highlight our forecast for the next pre-

dicted images of SNe Requiem and Encore. The study which discovered SN Requiem [27] predicted a ~ 20 year time delay, with the next images appearing in the mid to late 2030s. Our results differ significantly, implying a baseline of roughly 12 years, with SNe Requiem and Encore likely reappearing in 2027-2028 and 2033-2034, respectively. These predictions use a fixed cosmology with $H_0 = 67.7 \text{ km s}^{-1} \text{ Mpc}^{-1}$; a larger expansion rate would shorten these time delays. Observations of these images would enable a time-delay measurement of the Hubble constant of unprecedented precision from a single system. Monitoring for the reappearance of SN Requiem could therefore provide enormous benefit to cosmology sooner than previously expected.

This work is the first to leverage spatially resolved stellar kinematics to model the MACSJ0138 cluster. While the kinematics map measured in this work was computed from MUSE observations, there exist newer, deeper MUSE observations on this system. Future work leveraging these data has enormous potential, especially given recent progress in rigorously characterizing the use of stellar kinematics for time-delay lenses [59, 61, 63]. Our model contributes to the growing body of published mass models on MACSJ0138 [27, 32, 34, 35], a remarkable lens system enabling an enormous variety of science.

ACKNOWLEDGMENTS

We gratefully acknowledge helpful correspondence and feedback from Andrew Robertson, Anowar Shajib, Michele Cappellari, Ana Acebron, and Sherry Suyu.

This work utilized data from the ESO Science Archive Facility with DOI: <https://doi.eso.org/10.18727/archive/41>.

This work made extensive use of standard, open-source Python packages. In addition to those noted throughout the text, these include `astropy` [80–82], `numpy` [83], `scipy` [84], and `matplotlib` [85]. Additionally, we acknowledge use of the lux supercomputer at UC Santa Cruz, funded by NSF MRI grant AST 1828315.

Appendix A: Isothermal Jeans modeling

To describe the effect of SIDM on the cluster density profile, we utilize the isothermal Jeans formalism briefly described above in Section III A 1. This results in a piecewise DM density profile:

$$\rho_{\text{SIDM}}(r) = \begin{cases} \rho_{\text{iso}}(r) & r < r_1 \\ \rho_{\text{NFW}}(r) & r > r_1 \end{cases} \quad (\text{A1})$$

Where ρ_{NFW} denotes the usual Navarro-Frenk-White density profile, and ρ_{iso} describes the thermalized region, obeying the isothermal Jeans equation with an isothermal velocity of σ_0 . We make the same assumption as

in [47] and [14] that the expected pairwise particle velocity is $\langle v_{\text{pair}} \rangle = \frac{4\sigma_0}{\sqrt{\pi}}$. The SIDM cross sections in this work are reported as $\sigma/m = \langle \frac{\sigma v}{m} \rangle \langle v_{\text{pair}} \rangle^{-1}$ (c.f. Sagunski *et al.* [14] eq. 6). To ensure consistency with the outer NFW halo, boundary conditions are enforced at r_1 : the enclosed mass $M(< r_1)$ and density $\rho(r)$ are identical to an NFW halo.

We use a similar change of variables as in Section 2.2 of Robertson *et al.* [47], modified to account for the contribution of a baryonic density profile $\rho_b(r)$. From the Jeans equation for a thermalized DM profile ρ_{iso} ,

$$\frac{d}{dr} \left(r^2 \frac{d \ln \rho_{\text{iso}}}{dr} \right) = - \frac{4\pi G r^2 (\rho_{\text{iso}} + \rho_b)}{\sigma_0^2} \quad (\text{A2})$$

we introduce the change of variables $x = r/r_1$, $y = \ln(\rho_{\text{iso}}/\rho_0)$, $N_0 = \rho_0/\rho_1$, yielding:

$$\frac{d^2 y}{dx^2} = - \frac{2}{x} \frac{dy}{dx} - C \left(e^y + \frac{\rho_b(xr_1)}{\rho_0} \right) \quad (\text{A3})$$

$$C = \frac{4\pi G \rho_1 r_1^2 N_0}{\sigma_0^2} \quad (\text{A4})$$

To numerically solve the equation above for $\rho_{\text{iso}}(r)$, we use the `scipy` function `solve_bvp`. This solver simultaneously fits the above ODE and the free parameters N_0 and σ_0 , subject to the following boundary conditions:

$$\begin{aligned} y|_{x=0} &= 0 & M|_{x=0} &= 0 \\ \frac{dy}{dx}|_{x=0} &= 0 & y|_{x=1} &= -\ln(N_0) \\ M|_{x=1} &= M_{\text{NFW}}(< r_1) \end{aligned}$$

As may be apparent from the discussion above, the SIDM cross section σ/m is not directly sampled. Rather, the SIDM parameters are computed from Υ_* , M_{200m} , c_{200m} , and the radius r_1 . (This sampling via r_1 is termed the ‘outside-in’ method in Robertson *et al.* [47], as opposed to the ‘inside-out’ method computing directly from σ/m .) This poses a problem: since σ/m is a derived parameter, we can only place a prior on r_1 , rather than σ/m . We desire a flat prior on $\ln(\sigma/m)$, which would imply the following prior on $\ln r_1$:

$$P(\ln r_1) = \frac{d(\sigma/m)}{dr_1} \frac{r_1}{\sigma/m} \quad (\text{A5})$$

Though we sample from a flat prior $P(\ln r_1) = \text{const}$, we enforce our desired prior by adding a weighting $\ln \left(\frac{d(\sigma/m)}{dr_1} \frac{r_1}{\sigma/m} \right)$ to the log likelihood.

Appendix B: Triaxiality and Concentration Bias

While it is well known that strong lensing selected halos are biased to high concentrations, they additionally exhibit a severe triaxial bias: halos elongated along the line-of-sight are more likely to exhibit strong lensing. In addition, this triaxial bias is likely to artificially inflate the apparent concentration of lens halos, potentially as much as +60% (Andrade *et al.* [15], Appendix C).

We allow for an elliptical halo in three dimensions, rather than limiting ellipticity to the plane of the sky. We modify both our strong lensing and stellar kinematics models accordingly. The majority of cluster halos in the universe are expected to be roughly prolate [86]; as such, we allow for a prolate, rather than oblate or fully triaxial ellipticity. (In addition, the axisymmetric solutions of JAM, used for kinematics modeling, only allow for oblate or prolate halos, not fully triaxial.)

The introduction of a 3D ellipticity to matter halos is rarely treated with the subtlety it deserves. Andrade *et al.* [15] marginalizes over LOS ellipticity by inflating the lensing convergence $\kappa_e(\theta) = \kappa(\theta)/s$, for an axis ratio $s < 1$. While this correctly inflates the observed lensing, the mass and concentration of the halo are no longer meaningful: the apparent lensing now corresponds to a halo of mass M/s . Likewise, a common approach takes a spherical density profile $\rho_{\text{sph}}(r)$, and introduces an elliptical radius $r_e^2 = \frac{x^2}{q^2} + \frac{y^2}{q^2} + z^2$ such that $\rho_e(\vec{x}) = \rho_{\text{sph}}(r_e)$.⁷ However, this similarly fails to preserve important properties of the halo: the total halo mass is now $M_e = q^2 M_{\text{sph}}$.

In order to preserve the spherical overdensity (SO) halo definition for elliptical halos, and therefore the meaning of the mass and concentration (M_Δ, c_Δ), we introduce ellipticity as follows. A SO halo of volume $V_\Delta = \frac{4\pi}{3} R_\Delta^3$ has a mass of $M_\Delta = \Delta V_\Delta \rho_b(z)$, where $\rho_b(z)$ is a background density, commonly taken to be either the mean matter density $\rho_m(z)$ or the critical density of the universe $\rho_c(z)$, and Δ is the overdensity of the halo within R_Δ compared to this reference. We wish to preserve $V_{\Delta,e} = V_{\Delta,\text{sph}}$ and $M_{\Delta,e} = M_{\Delta,\text{sph}}$. For a prolate halo with axis ratio $q_{3d} < 1$, this requires:

$$r_e^2 = \frac{x^2}{q^{2/3}} + \frac{y^2}{q^{2/3}} + q^{4/3} z^2 \quad (\text{B1})$$

$$\rho_e(\vec{x}) = \rho_{\text{sph}}(r_e) \quad (\text{B2})$$

Where the major axis is aligned with the z -axis. We introduce an angle i between z and the LOS, such that z' becomes the true LOS and the observed coordinates on the sky are (x', y') . Strong lensing, however, is dependent on the projected mass density $\Sigma(x', y') =$

⁷ For $q < 1$, this corresponds to a prolate (‘pickle’-shaped) halo, and for $q > 1$ this represents an oblate (‘pancake’-shaped) halo.

$\int \rho(x', y', z') dz'$. We will use lowercase r to represent spherical 3D radii, and distinguish projected 2D radii with a capital R . The projected mass density of our prolate halo is therefore:

$$\Sigma_e(R_e) = \frac{q_{3d}^{1/3}}{\sqrt{\sin^2 i + q_{3d}^2 \cos^2 i}} \Sigma_{\text{sph}}(R_e) \quad (\text{B3})$$

$$R_e^2 = \frac{x'^2}{q_{3d}^{2/3}} + \frac{q_{3d}^{4/3} y'^2}{\sin^2 i + q_{3d}^2 \cos^2 i} \quad (\text{B4})$$

$$q_{2d} = \frac{q_{3d}}{\sqrt{\sin^2 i + q_{3d}^2 \cos^2 i}} \quad (\text{B5})$$

Where Σ_{sph} is the projected density for a spherical halo, and q_{2d} is the apparent projected ellipticity.⁸ For any basis function for a spherically symmetric, 3D density $\rho(r; s)$ with a scale radius s , and corresponding projected density $\Sigma_{\text{sph}}(R; s)$, 3D ellipticity can thus be trivially introduced by Eqs. B3-B5. We take advantage of this property to approximate our 3D, elliptical DM halo as a sum of Cored Steep Ellipsoids (CSEs) or Gaussians, in order to model the observed lensing and dynamics, respectively. See Sections IIIB and IIIC.

Appendix C: Robustness of the Measured Stellar Kinematics

Measurements of stellar kinematics can be highly sensitive to analysis choices, and we have drawn on recent work, particularly [59, 61], to ensure our measurements are as robust as possible. To illustrate the quality of our spectral fits, two sample `ppxf` fits in this work are shown in Figure 16. These demonstrate both the overall fit to the entire BCG used to determine an optimal spectral template, and a characteristic fit to an individual Voronoi bin.

The relative uncertainty of the stellar velocity dispersion measured in each Voronoi bin is shown in Figure 17. Total uncertainty is of order $\sim 10\%$ in each bin, and systematic uncertainty is subdominant to statistical uncertainty in all bins save for bin 9, the northernmost bin. Knabel *et al.* [61] has rigorously explored systematic uncertainty in similar measurements with the goal of sub-percent precision σ_v measurements, and demonstrated that the choice of stellar template library is often the dominant source of systematic uncertainty. In this work we exclusively used the XSL template library, limiting our ability to characterize this uncertainty. However, the same paper demonstrated such an effect on measurements using MUSE spectra was typically of order $\approx 3 - 4\%$, well below the statistical uncertainty in this

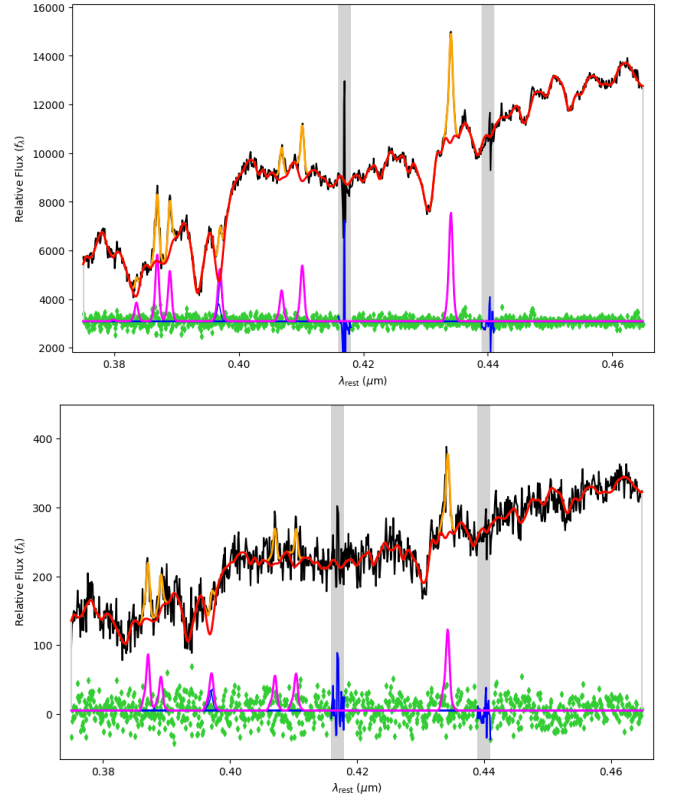


FIG. 16. Example `ppxf` fit results. Black represents data, red represents stellar model fit, orange represents stellar + gas model fit. **Top:** An example ‘total’ fit to all Voronoi bins combined, used to determine the optimal stellar template. Fit yielded a reduced χ^2 of 1.62. **Bottom:** An example fit to an individual Voronoi bin. This fit yielded a reduced χ^2 of 1.01.

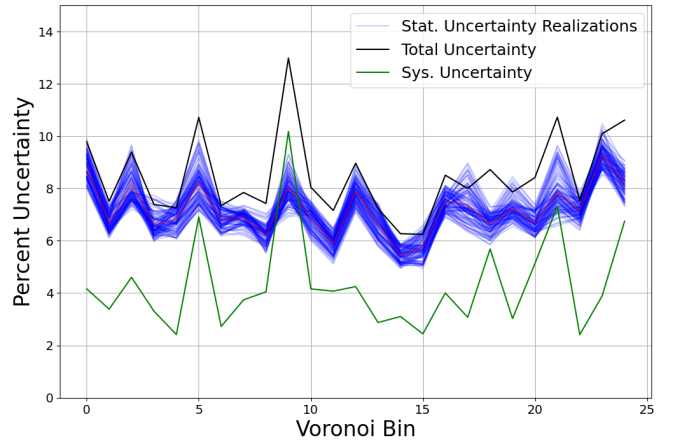


FIG. 17. Relative uncertain of the velocity dispersions measured in this work, for each voronoi bin. The total (systematic + statistical) uncertainty is shown in black; the statistical uncertainties of all 108 realizations described in Section IIIC 2 are shown in blue; and the systematic uncertainty is shown in green.

⁸ Compare Eq. B5 to Cappellari [69] Eq. 36.

work, and of similar scale to the systematic uncertainty we observe. However, our statistical uncertainty is large compared to [59, 61] in part because we use a less stringent SNR target inspired by [18]. A higher target spectral SNR threshold would yield fewer Voronoi bins, with

lower statistical uncertainties. We conducted several informal tests varying the spatial mask used to Voronoi bin the BCG, and increasing the spectral SNR target: in all cases, the kinematics maps produced were qualitatively consistent with the fiducial map used in this work.

-
- [1] S. Tulin and H.-B. Yu, Dark matter self-interactions and small scale structure, *Physics Reports* **730**, 1 (2018).
 - [2] S. Adhikari, A. Banerjee, K. K. Boddy, F.-Y. Cyr-Racine, H. Desmond, C. Dvorkin, B. Jain, F. Kahlhoefer, M. Kaplinghat, A. Nierenberg, A. H. G. Peter, A. Robertson, J. Sakstein, and J. Zavala, Astrophysical Tests of Dark Matter Self-Interactions, arXiv e-prints, arXiv:2207.10638 (2022), arXiv:2207.10638 [astro-ph.CO].
 - [3] J. L. Feng, M. Kaplinghat, and H.-B. Yu, Halo-Shape and Relic-Density Exclusions of Sommerfeld-Enhanced Dark Matter Explanations of Cosmic Ray Excesses, *Phys. Rev. Lett.* **104**, 151301 (2010), arXiv:0911.0422 [hep-ph].
 - [4] S. A. Khrapak, A. V. Ivlev, G. E. Morfill, and S. K. Zhdanov, Scattering in the attractive yukawa potential in the limit of strong interaction, *Phys. Rev. Lett.* **90**, 225002 (2003).
 - [5] W. J. G. de Blok, The Core-Cusp Problem, *Advances in Astronomy* **2010**, 789293 (2010), arXiv:0910.3538 [astro-ph.CO].
 - [6] K. A. Oman *et al.*, The unexpected diversity of dwarf galaxy rotation curves, *Mon. Not. Roy. Astron. Soc.* **452**, 3650 (2015), arXiv:1504.01437 [astro-ph.GA].
 - [7] N. J. Outmezguine, K. K. Boddy, S. Gad-Nasr, M. Kaplinghat, and L. Sagunski, Universal gravothermal evolution of isolated self-interacting dark matter halos for velocity-dependent cross-sections, *Monthly Notices of the Royal Astronomical Society* **523**, 4786 (2023), arXiv:2204.06568 [astro-ph.GA].
 - [8] J. Pollack, D. N. Spergel, and P. J. Steinhardt, Supermassive black holes from ultra-strongly self-interacting dark matter, *The Astrophysical Journal* **804**, 131 (2015).
 - [9] M. Grant Roberts, L. Braff, A. Garg, S. Profumo, T. Jeltema, and J. O'Donnell, Early formation of supermassive black holes from the collapse of strongly self-interacting dark matter, *Journal of Cosmology and Astroparticle Physics* **2025** (1), 060, arXiv:2410.17480 [astro-ph.GA].
 - [10] J. Choquette, J. M. Cline, and J. M. Cornell, Early formation of supermassive black holes via dark matter self-interactions, *Journal of Cosmology and Astroparticle Physics* **2019** (7), 036, arXiv:1812.05088 [astro-ph.CO].
 - [11] W.-X. Feng, H.-B. Yu, and Y.-M. Zhong, Seeding supermassive black holes with self-interacting dark matter: A unified scenario with baryons, *The Astrophysical Journal Letters* **914**, L26 (2021).
 - [12] A. Ragagnin, M. Meneghetti, F. Calura, G. Despali, K. Dolag, M. S. Fischer, C. Giocoli, and L. Moscardini, Dianoga SIDM: Galaxy cluster self-interacting dark matter simulations, *Astronomy and Astrophysics* **687**, A270 (2024).
 - [13] C. Mastromarino, G. Despali, L. Moscardini, A. Robertson, M. Meneghetti, and M. Maturi, Properties and observables of massive galaxies in self-interacting dark matter cosmologies, *Monthly Notices of the Royal Astronomical Society* **524**, 1515 (2023).
 - [14] L. Sagunski, S. Gad-Nasr, B. Colquhoun, A. Robertson, and S. Tulin, Velocity-dependent self-interacting dark matter from groups and clusters of galaxies, *Journal of Cosmology and Astroparticle Physics* **2021**, 024.
 - [15] K. E. Andrade, J. Fuson, S. Gad-Nasr, D. Kong, Q. Minor, M. G. Roberts, and M. Kaplinghat, A stringent upper limit on dark matter self-interaction cross-section from cluster strong lensing, *Monthly Notices of the Royal Astronomical Society* **510**, 54 (2022).
 - [16] T. Ren, A. Kwa, M. Kaplinghat, and H.-B. Yu, Reconciling the Diversity and Uniformity of Galactic Rotation Curves with Self-Interacting Dark Matter, *Physical Review X* **9**, 031020 (2019), arXiv:1808.05695 [astro-ph.GA].
 - [17] M. G. Roberts, M. Kaplinghat, M. Valli, and H.-B. Yu, Gravothermal collapse and the diversity of galactic rotation curves, *Physical Review D* **111**, 103041 (2025).
 - [18] A. B. Newman, T. Treu, R. S. Ellis, D. J. Sand, C. Nipoti, J. Richard, and E. Jullo, The Density Profiles of Massive, Relaxed Galaxy Clusters. I. The Total Density Over Three Decades in Radius, *The Astrophysical Journal* **765**, 24 (2013).
 - [19] A. B. Newman, T. Treu, R. S. Ellis, and D. J. Sand, The Density Profiles of Massive, Relaxed Galaxy Clusters. II. Separating Luminous and Dark Matter in Cluster Cores, *The Astrophysical Journal* **765**, 25 (2013).
 - [20] C. Cerny, M. Jauzac, D. Lagattuta, A. Niemiec, G. Mahler, A. Edge, and R. Massey, The Kaleidoscope Survey: Strong Gravitational Lensing in Galaxy Clusters with Radial Arcs (2025), arXiv:2506.21531 [astro-ph].
 - [21] D. Wittman, R. Stancoli, K. Finner, F. Bouhrik, R. van Weeren, and A. Botteon, A New Galaxy Cluster Merger Capable of Probing Dark Matter: A56, *The Astrophysical Journal* **954**, 36 (2023).
 - [22] D. Cross, G. Thoron, T. E. Jeltema, A. Swart, D. L. Hollowood, S. Adhikari, S. Bocquet, O. Eiger, S. Everett, J. Jobel, D. Laubner, A. McDaniel, M. Agüena, O. Alves, F. Andrade-Oliveira, D. Bacon, E. Bertin, D. Brooks, D. L. Burke, A. Carnero Rosell, M. Carrasco Kind, R. Cawthon, M. Costanzi, L. N. da Costa, M. E. S. Pereira, T. M. Davis, S. Desai, P. Doel, I. Ferrero, J. Frieman, J. García-Bellido, G. Giannini, D. Gruen, R. A. Gruendl, S. R. Hinton, K. Honscheid, D. J. James, K. Kuehn, J. L. Marshall, J. Mena-Fernández, F. Menanteau, R. Miquel, R. L. C. Ogando, A. Pieres, A. A. Plazas Malagón, M. Raveri, A. K. Romer, E. Sanchez, I. Sevilla-Noarbe, M. Smith, M. Soares-Santos, F. Sobreira, E. Suchyta, M. E. C. Swanson, G. Tarle, C. To, N. Weaverdyck, J. Weller, P. Wiseman, and (DES Collaboration), Examining the self-interaction of dark matter through central cluster galaxy offsets, *Monthly Notices of the Royal Astronomical Society* **529**, 52 (2024).
 - [23] D. Harvey, A. Robertson, R. Massey, and I. G. Mc-

- Carthy, Observable tests of self-interacting dark matter in galaxy clusters: BCG wobbles in a constant density core, *Monthly Notices of the Royal Astronomical Society* **488**, 1572 (2019).
- [24] S.-I. Tam, K. Umetsu, A. Robertson, and I. G. McCarthy, Testing the Collisionless Nature of Dark Matter with the Radial Acceleration Relation in Galaxy Clusters, *The Astrophysical Journal* **953**, 169 (2023).
- [25] A. Robertson, E. Huff, and K. Marković, Why weak lensing cluster shapes are insensitive to self-interacting dark matter, *Monthly Notices of the Royal Astronomical Society* **521**, 3172 (2023).
- [26] E. J. Gonzalez, A. Rodríguez-Medrano, L. Pereyra, and D. García Lambas, Cluster halo shapes in CDM and SIDM models: Unveiling the DM particle nature using a weak-lensing approach, *Monthly Notices of the Royal Astronomical Society* **528**, 3075 (2024).
- [27] S. A. Rodney, G. B. Brammer, J. D. R. Pierel, J. Richard, S. Toft, K. F. O'Connor, M. Akhshik, and K. E. Whitaker, A gravitationally lensed supernova with an observable two-decade time delay, *Nature Astronomy* **10.1038/s41550-021-01450-9** (2021).
- [28] J. D. R. Pierel, A. B. Newman, S. Dhawan, M. Gu, B. A. Joshi, T. Li, S. Schuldt, L. G. Strolger, S. H. Suyu, G. B. Caminha, S. H. Cohen, J. M. Diego, J. C. J. D'Silva, S. Ertl, B. L. Frye, G. Granata, C. Grillo, A. M. Koekemoer, J. Li, A. Robotham, J. Summers, T. Treu, R. A. Windhorst, A. Zitrin, S. Agarwal, A. Agrawal, N. Arendse, S. Belli, C. Burns, R. Cañameras, S. Chakrabarti, W. Chen, T. E. Collett, D. A. Coulter, R. S. Ellis, M. Engesser, N. Foo, O. D. Fox, C. Gall, N. Garuda, S. Gezari, S. Gomez, K. Glazebrook, J. Hjorth, X. Huang, S. W. Jha, P. S. Kamienieski, P. Kelly, C. Larison, L. A. Moustakas, M. Pascale, I. Pérez-Fournon, T. Petrushevska, F. Poidevin, A. Rest, M. Shahbandeh, A. J. Shajib, M. Siebert, C. Storer, M. Talbot, Q. Wang, T. Wevers, and Y. Zenati, Lensed Type Ia Supernova "Encore" at $z = 2$: The First Instance of Two Multiply Imaged Supernovae in the Same Host Galaxy, *The Astrophysical Journal* **967**, L37 (2024).
- [29] A. Flowers, J. H. O'Donnell, T. E. Jeltema, V. Wetzell, and M. G. Roberts, Spectroscopic and X-ray Modeling of the Strong Lensing Galaxy Cluster MACS J0138.0-2155, *The Open Journal of Astrophysics* **8**, 75 (2025).
- [30] G. Granata, G. B. Caminha, S. Ertl, C. Grillo, S. Schuldt, S. H. Suyu, A. Acebron, P. Bergamini, R. Cañameras, A. M. Koekemoer, P. Rosati, and S. Taubenberger, Cosmology with supernova Encore in the strong lensing cluster MACS J0138-2155: Spectroscopy with MUSE, *Astronomy and Astrophysics* **697**, A94 (2025).
- [31] S. Dhawan, J. D. R. Pierel, M. Gu, A. B. Newman, C. Larison, M. Siebert, T. Petrushevska, F. Poidevin, S. W. Jha, W. Chen, R. S. Ellis, B. Frye, J. Hjorth, A. M. Koekemoer, I. Pérez-Fournon, A. Rest, T. Treu, R. A. Windhorst, and Y. Zenati, Spectroscopic analysis of the strongly lensed SN Encore: Constraints on cosmic evolution of Type Ia supernovae, *Monthly Notices of the Royal Astronomical Society* **535**, 2939 (2024).
- [32] A. B. Newman, S. Belli, R. S. Ellis, and S. G. Patel, Resolving Quiescent Galaxies at $z \geq 2$. I. Search for Gravitationally Lensed Sources and Characterization of Their Structure, Stellar Populations, and Line Emission, *The Astrophysical Journal* **862**, 125 (2018).
- [33] A. B. Newman, M. Gu, S. Belli, R. S. Ellis, S. Gangula, J. E. Greene, J. L. Walsh, S. H. Suyu, S. Ertl, G. Caminha, G. Granata, C. Grillo, S. Schuldt, T. M. Barone, S. Bird, K. Glazebrook, M. Jafariyazani, M. Kriek, A. Matthews, T. Morishita, T. Nanayakkara, J. D. R. Pierel, A. Acebron, P. Bergamini, S. Cha, J. M. Diego, N. Foo, B. Frye, Y. Fudamoto, M. J. Jee, P. S. Kamienieski, A. M. Koekemoer, A. K. Meena, S. Nishida, M. Oguri, P. Rosati, and A. Zitrin, A stellar dynamical mass measure of an inactive black hole in the distant universe (2025).
- [34] S. Ertl, S. H. Suyu, S. Schuldt, G. Granata, C. Grillo, G. B. Caminha, A. Acebron, P. Bergamini, R. Cañameras, S. Cha, J. M. Diego, N. Foo, B. L. Frye, Y. Fudamoto, A. Halkola, M. J. Jee, P. S. Kamienieski, A. M. Koekemoer, A. K. Meena, S. Nishida, M. Oguri, J. D. R. Pierel, P. Rosati, L. Tortorelli, H. Wang, and A. Zitrin, Cosmology with Supernova Encore in the strong lensing cluster MACS J0138-2155: Photometry, cluster members, and lens mass model (2025), arXiv:2503.09718 [astro-ph].
- [35] A. Acebron, P. Bergamini, P. Rosati, P. Tozzi, M. Meneghetti, G. B. Caminha, S. Ertl, G. Granata, A. M. Koekemoer, C. Grillo, S. Schuldt, B. L. Frye, and J. M. Diego, Enhanced strong-lensing model of MACS J0138.0-2155 based on new JWST and VLT/MUSE observations, *Astronomy and Astrophysics* **699**, A101 (2025).
- [36] R. Bacon, M. Accardo, L. Adjali, H. Anwand, S. Bauer, I. Biswas, J. Blaizot, D. Boudon, S. Brau-Nogue, J. Brinchmann, P. Caillier, L. Capolani, C. M. Carollo, T. Contini, P. Couderc, E. Daguisé, S. Deiries, B. Delabre, S. Dreizler, J. Dubois, M. Dupieux, C. Dupuy, E. Emsellem, T. Fechner, A. Fleischmann, M. François, G. Gallou, T. Gharsa, A. Glindemann, D. Gojak, B. Guiderdoni, G. Hansali, T. Hahn, A. Jarno, A. Kelz, C. Koehler, J. Kosmalski, F. Laurent, M. Le Floch, S. J. Lilly, J. L. Lizon, M. Loupias, A. Manescau, C. Monstein, H. Nicklas, J. C. Olaya, L. Pares, L. Pasquini, A. Pécontal-Rousset, R. Pelló, C. Petit, E. Popow, R. Reiss, A. Remillieux, E. Renault, M. Roth, G. Rupprecht, D. Serre, J. Schaye, G. Soucail, M. Steinmetz, O. Streicher, R. Stuik, H. Valentin, J. Vernet, P. Weilbacher, L. Wisotzki, and N. Yerle, The MUSE second-generation VLT instrument, in *Ground-based and Airborne Instrumentation for Astronomy III*, Society of Photo-Optical Instrumentation Engineers (SPIE) Conference Series, Vol. 7735, edited by I. S. McLean, S. K. Ramsay, and H. Takami (2010) p. 773508, arXiv:2211.16795 [astro-ph.IM].
- [37] P. M. Weilbacher, R. Palsa, O. Streicher, R. Bacon, T. Urrutia, L. Wisotzki, S. Conseil, B. Husemann, A. Jarno, A. Kelz, A. Pécontal-Rousset, J. Richard, M. M. Roth, F. Selman, and J. Vernet, The data processing pipeline for the MUSE instrument, *Astronomy and Astrophysics* **641**, A28 (2020).
- [38] J. W. Nightingale, S. Dye, and R. J. Massey, AutoLens: Automated modeling of a strong lens's light, mass, and source, *MNRAS* **478**, 4738 (2018), arXiv:1708.07377.
- [39] J. W. Nightingale, R. J. Massey, D. R. Harvey, A. P. Cooper, A. Etherington, S. I. Tam, and R. G. Hayes, Galaxy structure with strong gravitational lensing: Decomposing the internal mass distribution of massive elliptical galaxies, *MNRAS* **489**, 2049 (2019), arXiv:1901.07801.

- [40] M. Cappellari and Y. Copin, Adaptive spatial binning of integral-field spectroscopic data using Voronoi tessellations, *Monthly Notices of the Royal Astronomical Society* **342**, 345 (2003).
- [41] M. Cappellari and E. Emsellem, Parametric Recovery of Line-of-Sight Velocity Distributions from Absorption-Line Spectra of Galaxies via Penalized Likelihood, *Publications of the Astronomical Society of the Pacific* **116**, 138 (2004).
- [42] M. Cappellari, Improving the full spectrum fitting method: Accurate convolution with Gauss-Hermite functions, *Monthly Notices of the Royal Astronomical Society* **466**, 798 (2017).
- [43] M. Cappellari, Efficient multi-Gaussian expansion of galaxies, *Monthly Notices of the Royal Astronomical Society* **333**, 400 (2002).
- [44] M. Cappellari, Measuring the inclination and mass-to-light ratio of axisymmetric galaxies via anisotropic Jeans models of stellar kinematics, *Monthly Notices of the Royal Astronomical Society* **390**, 71 (2008).
- [45] M. Cappellari, Anisotropic Jeans models of stellar kinematics: Second moments including proper motions and radial velocities (2012).
- [46] M. Vogelsberger, J. Zavala, C. Simpson, and A. Jenkins, Dwarf galaxies in CDM and SIDM with baryons: Observational probes of the nature of dark matter, *Monthly Notices of the Royal Astronomical Society* **444**, 3684 (2014).
- [47] A. Robertson, R. Massey, V. Eke, J. Schaye, and T. Theuns, The surprising accuracy of isothermal Jeans modelling of self-interacting dark matter density profiles, *Monthly Notices of the Royal Astronomical Society* **501**, 4610 (2021).
- [48] M. R. Blanton and S. Roweis, K-Corrections and Filter Transformations in the Ultraviolet, Optical, and Near-Infrared, *The Astronomical Journal* **133**, 734 (2007).
- [49] A. Dey, D. J. Schlegel, D. Lang, R. Blum, K. Burleigh, X. Fan, J. R. Findlay, D. Finkbeiner, D. Herrera, S. Juneau, M. Landriau, M. Levi, I. McGreer, A. Meisner, A. D. Myers, J. Moustakas, P. Nugent, A. Patej, E. F. Schlafly, A. R. Walker, F. Valdes, B. A. Weaver, C. Yèche, H. Zou, X. Zhou, B. Abareschi, T. M. C. Abbott, B. Abolfathi, C. Aguilera, S. Alam, L. Allen, A. Alvarez, J. Annis, B. Ansarinejad, M. Aubert, J. Beechert, E. F. Bell, S. Y. BenZvi, F. Beutler, R. M. Bielby, A. S. Bolton, C. Briceño, E. J. Buckley-Geer, K. Butler, A. Calamida, R. G. Carlberg, P. Carter, R. Casas, F. J. Castander, Y. Choi, J. Comparat, E. Cukanovaite, T. Delubac, K. DeVries, S. Dey, G. Dhungana, M. Dickinson, Z. Ding, J. B. Donaldson, Y. Duan, C. J. Duckworth, S. Eftekharzadeh, D. J. Eisenstein, T. Etourneau, P. A. Fagrelus, J. Farihi, M. Fitzpatrick, A. Font-Ribera, L. Fulmer, B. T. Gänsicke, E. Gaztanaga, K. George, D. W. Gerdes, S. G. A. Gontcho, C. Gorgoni, G. Green, J. Guy, D. Harmer, M. Hernandez, K. Honscheid, L. W. Huang, D. J. James, B. T. Jannuzi, L. Jiang, R. Joyce, A. Karcher, S. Karkar, R. Kehoe, J.-P. Kneib, A. Kueter-Young, T.-W. Lan, T. R. Lauer, L. Le Guillou, A. Le Van Suu, J. H. Lee, M. Lesser, L. Perreault Levasseur, T. S. Li, J. L. Mann, R. Marshall, C. E. Martínez-Vázquez, P. Martini, H. du Mas des Bourboux, S. McManus, T. G. Meier, B. Ménard, N. Metcalfe, A. Muñoz-Gutiérrez, J. Najita, K. Napier, G. Narayan, J. A. Newman, J. Nie, B. Nord, D. J. Norman, K. A. G. Olsen, A. Paat, N. Palanque-Delabrouille, X. Peng, C. L. Poppe, M. R. Poremba, A. Prakash, D. Rabinowitz, A. Raichoor, M. Rezaie, A. N. Robertson, N. A. Roe, A. J. Ross, N. P. Ross, G. Rudnick, S. Safonova, A. Saha, F. J. Sánchez, E. Savary, H. Schweiker, A. Scott, H.-J. Seo, H. Shan, D. R. Silva, Z. Slepian, C. Soto, D. Sprayberry, R. Staten, C. M. Stillman, R. J. Stupak, D. L. Summers, S. Sien Tie, H. Tirado, M. Vargas-Magaña, A. K. Vivas, R. H. Wechsler, D. Williams, J. Yang, Q. Yang, T. Yapici, D. Zaritsky, A. Zenteno, K. Zhang, T. Zhang, R. Zhou, and Z. Zhou, Overview of the DESI Legacy Imaging Surveys, *The Astronomical Journal* **157**, 168 (2019).
- [50] J. W. Nightingale, R. G. Hayes, A. Kelly, A. Amvrosiadis, A. Etherington, Q. He, N. Li, X. Cao, J. Frawley, S. Cole, A. Enia, C. S. Frenk, D. R. Harvey, R. Li, R. J. Massey, M. Negrello, and A. Robertson, ‘pyautolens’: Open-source strong gravitational lensing, *J. Open Source Softw.* **6**, 2825 (2021).
- [51] E. Jullo, J.-P. Kneib, M. Limousin, Á. Elíasdóttir, P. J. Marshall, and T. Verdugo, A Bayesian approach to strong lensing modelling of galaxy clusters, *New Journal of Physics* **9**, 447 (2007).
- [52] J.-P. Kneib, H. Bonnet, G. Golse, D. Sand, E. Jullo, and P. Marshall, LENSTOOL: A Gravitational Lensing Software for Modeling Mass Distribution of Galaxies and Clusters (strong and weak regime), *Astrophysics Source Code Library*, ascl:1102.004 (2011).
- [53] Á. Elíasdóttir, M. Limousin, J. Richard, J. Hjorth, J.-P. Kneib, P. Natarajan, K. Pedersen, E. Jullo, and D. Paraficz, Where is the matter in the Merging Cluster Abell 2218?, *arXiv:0710.5636 [astro-ph]* (2007), *arXiv:0710.5636 [astro-ph]*.
- [54] M. Oguri, Fast Calculation of Gravitational Lensing Properties of Elliptical Navarro-Frenk-White and Hernquist Density Profiles, *Publications of the Astronomical Society of the Pacific* **133**, 074504 (2021), *arXiv:2106.11464 [astro-ph.IM]*.
- [55] P. Bergamini, P. Rosati, A. Mercurio, C. Grillo, G. B. Caminha, M. Meneghetti, A. Agnello, A. Biviano, F. Calura, C. Giocoli, M. Lombardi, G. Rodighiero, and E. Vanzella, Enhanced cluster lensing models with measured galaxy kinematics, *Astronomy & Astrophysics*, Volume 631, id.A130, <NUMPAGES>16</NUMPAGES> pp. **631**, A130 (2019).
- [56] C. C. Gibson, J. H. O’Donnell, and T. E. Jeltema, A TALE OF TAILS: STAR FORMATION AND STRIPPING IN JELLYFISH GALAXIES IN THE STRONG LENSING CLUSTER MACS J0138.0-215, TBD (2025).
- [57] M. Lombardi, Gravity.jl: Fast and accurate gravitational lens modeling in Julia: I. Point-like and linearized extended sources, *Astronomy and Astrophysics* **690**, A346 (2024), *arXiv:2406.15280 [astro-ph.IM]*.
- [58] D. J. Sand, T. Treu, G. P. Smith, and R. S. Ellis, The Dark Matter Distribution in the Central Regions of Galaxy Clusters: Implications for Cold Dark Matter, *The Astrophysical Journal* **604**, 88 (2004).
- [59] A. J. Shajib, P. Mozumdar, G. C. F. Chen, T. Treu, M. Cappellari, S. Knabel, S. H. Suyu, V. N. Bennert, J. A. Frieman, D. Sluse, S. Birrer, F. Courbin, C. D. Fassnacht, L. Villafañá, and P. R. Williams, TDCOSMO. XII. Improved Hubble constant measurement from lensing time delays using spatially resolved stellar kinematics

- of the lens galaxy, *Astronomy and Astrophysics* **673**, A9 (2023).
- [60] S. Knabel, T. Treu, M. Cappellari, A. J. Shajib, C.-F. Chen, and V. N. Bennert, Spatially Resolved Kinematics of SLACS Lens Galaxies. I: Data and Kinematic Classification (2024), arXiv:2409.10631 [astro-ph].
- [61] S. Knabel, P. Mozumdar, A. J. Shajib, T. Treu, M. Cappellari, C. Spiniello, and S. Birrer, TDCOSMO XIX: Measuring stellar velocity dispersion with sub-percent accuracy for cosmography (2025), arXiv:2502.16034 [astro-ph].
- [62] S. Birrer, E. J. Buckley-Geer, M. Cappellari, F. Courbin, F. Dux, C. D. Fassnacht, J. A. Frieman, A. Galan, D. Gilman, X.-Y. Huang, S. Knabel, D. Langeroodi, H. Lin, M. Millon, T. Morishita, V. Motta, P. Mozumdar, E. Paic, A. J. Shajib, W. Sheu, D. Sluse, A. Sonnenfeld, C. Spiniello, M. Stiavelli, S. H. Suyu, C. Y. Tan, T. Treu, L. V. de Vyvere, H. Wang, P. Wells, D. M. Williams, and K. C. Wong, TDCOSMO 2025: Cosmological constraints from strong lensing time delays (2025), arXiv:2506.03023 [astro-ph].
- [63] A. J. Shajib, T. Treu, S. H. Suyu, D. Law, A. Yıldırım, M. Cappellari, A. Galan, S. Knabel, H. Wang, S. Birrer, F. Courbin, C. D. Fassnacht, J. A. Frieman, A. Melo, T. Morishita, P. Mozumdar, D. Sluse, and M. Stiavelli, TDCOSMO XXIII. First spatially resolved kinematics of the lens galaxy obtained using JWST-NIRSpec to improve time-delay cosmography (2025), arXiv:2506.21665 [astro-ph].
- [64] H. C. Turner, R. J. Smith, and T. E. Collett, Two-dimensional kinematics and dynamical modelling of the 'Jackpot' gravitational lens from deep MUSE observations, *Monthly Notices of the Royal Astronomical Society* **528**, 3559 (2024).
- [65] H. Wang, R. Cañameras, G. B. Caminha, S. H. Suyu, A. Yıldırım, G. Chirivì, L. Christensen, C. Grillo, and S. Schuldt, Constraining the multi-scale dark-matter distribution in CASSOWARY 31 with strong gravitational lensing and stellar dynamics, *Astronomy and Astrophysics* **668**, A162 (2022).
- [66] H. Wang, R. Cañameras, S. H. Suyu, A. Galan, C. Grillo, G. B. Caminha, and L. Christensen, Strong-lensing and kinematic analysis of CASSOWARY 31: Can strong lensing constrain the masses of multi-plane lenses?, *Astronomy and Astrophysics* **690**, A1 (2024).
- [67] K. Verro, S. C. Trager, R. F. Peletier, A. Lançon, A. Gonneau, A. Vazdekis, P. Prugniel, Y. P. Chen, P. R. T. Coelho, P. Sánchez-Blázquez, L. Martins, A. Arntsen, M. Lyubenova, J. Falcón-Barroso, and M. Dries, The X-shooter Spectral Library (XSL): Data Release 3, *Astronomy and Astrophysics* **660**, A34 (2022).
- [68] D. Calzetti, L. Armus, R. C. Bohlin, A. L. Kinney, J. Koornneef, and T. Storchi-Bergmann, The Dust Content and Opacity of Actively Star-forming Galaxies, *The Astrophysical Journal* **533**, 682 (2000).
- [69] M. Cappellari, Efficient solution of the anisotropic spherically aligned axisymmetric Jeans equations of stellar hydrodynamics for galactic dynamics, *Monthly Notices of the Royal Astronomical Society* **494**, 4819 (2020).
- [70] K. Zhu, S. Lu, M. Cappellari, R. Li, S. Mao, and L. Gao, MaNGA DynPop - I. Quality-assessed stellar dynamical modelling from integral-field spectroscopy of 10K nearby galaxies: A catalogue of masses, mass-to-light ratios, density profiles, and dark matter, *Monthly Notices of the Royal Astronomical Society* **522**, 6326 (2023).
- [71] Planck Collaboration, P. A. R. Ade, N. Aghanim, M. Arnaud, M. Ashdown, J. Aumont, C. Baccigalupi, A. J. Banday, R. B. Barreiro, J. G. Bartlett, N. Bartolo, E. Battaner, R. Battye, K. Benabed, A. Benoit, A. Benoit-Lévy, J. P. Bernard, M. Bersanelli, P. Bielewicz, J. J. Bock, A. Bonaldi, L. Bonavera, J. R. Bond, J. Borrill, F. R. Bouchet, F. Boulanger, M. Bucher, C. Burigana, R. C. Butler, E. Calabrese, J. F. Cardoso, A. Catalano, A. Challinor, A. Chambaullu, R. R. Chary, H. C. Chiang, J. Chluba, P. R. Christensen, S. Church, D. L. Clements, S. Colombi, L. P. L. Colombo, C. Combet, A. Coulais, B. P. Crill, A. Curto, F. Cuttaia, L. Danese, R. D. Davies, R. J. Davis, P. de Bernardis, A. de Rosa, G. de Zotti, J. Delabrouille, F. X. Désert, E. Di Valentino, C. Dickinson, J. M. Diego, K. Dolag, H. Dole, S. Donzelli, O. Doré, M. Douspis, A. Ducout, J. Dunkley, X. Dupac, G. Efstathiou, F. Elsner, T. A. Enßlin, H. K. Eriksen, M. Farhang, J. Fergusson, F. Finelli, O. Forni, M. Frailis, A. A. Fraisse, E. Franceschi, A. Frejsel, S. Galeotta, S. Galli, K. Ganga, C. Gauthier, M. Gerbino, T. Ghosh, M. Giard, Y. Giraud-Héraud, E. Giusarma, E. Gjerløw, J. González-Nuevo, K. M. Górski, S. Gratton, A. Gregorio, A. Gruppuso, J. E. Gudmundsson, J. Hamann, F. K. Hansen, D. Hanson, D. L. Harrison, G. Helou, S. Henrot-Versillé, C. Hernández-Monteagudo, D. Herranz, S. R. Hildebrandt, E. Hivon, M. Hobson, W. A. Holmes, A. Hornstrup, W. Hovest, Z. Huang, K. M. Hufenberger, G. Hurier, A. H. Jaffe, T. R. Jaffe, W. C. Jones, M. Juvela, E. Keihänen, R. Keskitalo, T. S. Kisner, R. Kneissl, J. Knoche, L. Knox, M. Kunz, J. H. Kurki-Suonio, G. Lagache, A. Lähteenmäki, J. M. Lamarre, A. Lasenby, M. Lattanzi, C. R. Lawrence, J. P. Leahy, R. Leonardi, J. Lesgourgues, F. Levrier, A. Lewis, M. Liguori, P. B. Lilje, M. Linden-Vørnle, M. López-Cañieago, P. M. Lubin, J. F. Macías-Pérez, G. Maggio, D. Maino, N. Mandolesi, A. Mangilli, A. Marchini, M. Maris, P. G. Martin, M. Martinelli, E. Martínez-González, S. Masi, S. Matarrese, P. McGehee, P. R. Meinhold, A. Melchiorri, J. B. Melin, L. Mendes, A. Mennella, M. Migliaccio, M. Millea, S. Mitra, M. A. Miville-Deschênes, A. Moneti, L. Montier, G. Morgante, D. Mortlock, A. Moss, D. Munshi, J. A. Murphy, P. Naselsky, F. Nati, P. Natoli, C. B. Netterfield, H. U. Nørgaard-Nielsen, F. Novello, D. Novikov, I. Novikov, C. A. Oxborrow, F. Paci, L. Pagano, F. Pajot, R. Paladini, D. Paoletti, B. Partridge, F. Pasian, G. Patanchon, T. J. Pearson, O. Perdereau, L. Perotto, F. Perrotta, V. Pettorino, F. Piacentini, M. Piat, E. Pierpaoli, D. Pietrobon, S. Plaszczynski, E. Pointecouteau, G. Polenta, L. Popa, G. W. Pratt, and G. Prézeau, Planck 2015 results. XIII. Cosmological parameters, *Astronomy and Astrophysics* **594**, A13 (2016).
- [72] D. Foreman-Mackey, D. W. Hogg, D. Lang, and J. Goodman, emcee: The MCMC Hammer, *Publications of the Astronomical Society of the Pacific* **125**, 306 (2013), arXiv:1202.3665 [astro-ph.IM].
- [73] J. Goodman and J. Weare, Ensemble samplers with affine invariance, *Communications in Applied Mathematics and Computational Science* **5**, 65 (2010).
- [74] B. Nelson, E. B. Ford, and M. J. Payne, RUN DMC: An Efficient, Parallel Code for Analyzing Radial Velocity Observations Using N-body Integrations and Differential Evolution Markov Chain Monte Carlo, *The Astrophysical*

- Journal Supplement Series **210**, 11 (2014).
- [75] C. J. F. Ter Braak, A Markov Chain Monte Carlo version of the genetic algorithm Differential Evolution: Easy Bayesian computing for real parameter spaces, *Statistics and Computing* **16**, 239 (2006).
 - [76] D. Foreman-Mackey, corner.py: Scatterplot matrices in python, *The Journal of Open Source Software* **1**, 24 (2016).
 - [77] B. Diemer, COLOSSUS: A Python Toolkit for Cosmology, Large-scale Structure, and Dark Matter Halos, *The Astrophysical Journal Supplement Series* **239**, 35 (2018).
 - [78] A. D. Ludlow, S. Bose, R. E. Angulo, L. Wang, W. A. Hellwing, J. F. Navarro, S. Cole, and C. S. Frenk, The mass-concentration-redshift relation of cold and warm dark matter haloes, *Monthly Notices of the Royal Astronomical Society* **460**, 1214 (2016).
 - [79] A. Etherington, J. W. Nightingale, R. Massey, S.-I. Tam, X. Cao, A. Niemiec, Q. He, A. Robertson, R. Li, A. Amvrosiadis, S. Cole, J. M. Diego, C. S. Frenk, B. L. Frye, D. Harvey, M. Jauzac, A. M. Koekemoer, D. J. Lagattuta, S. Lange, M. Limousin, G. Mahler, E. Sirks, and C. L. Steinhardt, Strong gravitational lensing's 'external shear' is not shear, *Monthly Notices of the Royal Astronomical Society* **531**, 3684 (2024).
 - [80] Astropy Collaboration, T. P. Robitaille, E. J. Tollerud, P. Greenfield, M. Droettboom, E. Bray, T. Aldcroft, M. Davis, A. Ginsburg, A. M. Price-Whelan, W. E. Kerzendorf, A. Conley, N. Crighton, K. Barbary, D. Muna, H. Ferguson, F. Grollier, M. M. Parikh, P. H. Nair, H. M. Unther, C. Deil, J. Woillez, S. Conseil, R. Kramer, J. E. H. Turner, L. Singer, R. Fox, B. A. Weaver, V. Zabalza, Z. I. Edwards, K. Azalee Bostroem, D. J. Burke, A. R. Casey, S. M. Crawford, N. Dencheva, J. Ely, T. Jenness, K. Labrie, P. L. Lim, F. Pierfederici, A. Pontzen, A. Ptak, B. Refsdal, M. Servillat, and O. Streicher, Astropy: A community Python package for astronomy, *Astronomy and Astrophysics* **558**, A33 (2013).
 - [81] Astropy Collaboration, A. M. Price-Whelan, B. M. Sipőcz, H. M. Günther, P. L. Lim, S. M. Crawford, S. Conseil, D. L. Shupe, M. W. Craig, N. Dencheva, A. Ginsburg, J. T. VanderPlas, L. D. Bradley, D. Pérez-Suárez, M. de Val-Borro, T. L. Aldcroft, K. L. Cruz, T. P. Robitaille, E. J. Tollerud, C. Ardelean, T. Babej, Y. P. Bach, M. Bachetti, A. V. Bakanov, S. P. Bamford, G. Barentsen, P. Barmby, A. Baumbach, K. L. Berry, F. Biscani, M. Boquien, K. A. Bostroem, L. G. Bouma, G. B. Brammer, E. M. Bray, H. Breytenbach, H. Buddelmeijer, D. J. Burke, G. Calderone, J. L. Cano Rodríguez, M. Cara, J. V. M. Cardoso, S. Cheedella, Y. Copin, L. Corrales, D. Crichton, D. D'Avella, C. Deil, E. Depagne, J. P. Dietrich, A. Donath, M. Droettboom, N. Earl, T. Erben, S. Fabbro, L. A. Ferreira, T. Finethy, R. T. Fox, L. H. Garrison, S. L. J. Gibbons, D. A. Goldstein, R. Gommers, J. P. Greco, P. Greenfield, A. M. Groener, F. Grollier, A. Hagen, P. Hirst, D. Homeier, A. J. Horton, G. Hosseinzadeh, L. Hu, J. S. Hunkeler, Ž. Ivezić, A. Jain, T. Jenness, G. Kanarek, S. Kendrew, N. S. Kern, W. E. Kerzendorf, A. Khvalko, J. King, D. Kirkby, A. M. Kulkarni, A. Kumar, A. Lee, D. Lenz, S. P. Littlefair, Z. Ma, D. M. Macleod, M. Mastroiello, C. McCully, S. Montagnac, B. M. Morris, M. Mueller, S. J. Mumford, D. Muna, N. A. Murphy, S. Nelson, G. H. Nguyen, J. P. Ninan, M. Nöthe, S. Ogaz, S. Oh, J. K. Parejko, N. Parley, S. Pascual, R. Patil, A. A. Patil, A. L. Plunkett, J. X. Prochaska, T. Rastogi, V. Reddy Janga, J. Sabater, P. Sakurikar, M. Seifert, L. E. Sherbert, H. Sherwood-Taylor, A. Y. Shih, J. Sick, M. T. Silbiger, S. Singanamalla, L. P. Singer, P. H. Sladen, K. A. Sooley, S. Sornarajah, O. Streicher, P. Teuben, S. W. Thomas, G. R. Tremblay, J. E. H. Turner, V. Terrón, M. H. van Kerkwijk, A. de la Vega, L. L. Watkins, B. A. Weaver, J. B. Whitmore, J. Woillez, V. Zabalza, and Astropy Contributors, The Astropy Project: Building an Open-science Project and Status of the v2.0 Core Package, *The Astronomical Journal* **156**, 123 (2018).
 - [82] Astropy Collaboration, A. M. Price-Whelan, P. L. Lim, N. Earl, N. Starkman, L. Bradley, D. L. Shupe, A. A. Patil, L. Corrales, C. E. Brasseur, M. Nöthe, A. Donath, E. Tollerud, B. M. Morris, A. Ginsburg, E. Vaher, B. A. Weaver, J. Tocknell, W. Jamieson, M. H. van Kerkwijk, T. P. Robitaille, B. Merry, M. Bachetti, H. M. Günther, T. L. Aldcroft, J. A. Alvarado-Montes, A. M. Archibald, A. Bódi, S. Bapat, G. Barentsen, J. Bazán, M. Biswas, M. Boquien, D. J. Burke, D. Cara, M. Cara, K. E. Conroy, S. Conseil, M. W. Craig, R. M. Cross, K. L. Cruz, F. D'Eugenio, N. Dencheva, H. A. R. Devillepoix, J. P. Dietrich, A. D. Eigenbrot, T. Erben, L. Ferreira, D. Foreman-Mackey, R. Fox, N. Freij, S. Garg, R. Geda, L. Glattly, Y. Gondhalekar, K. D. Gordon, D. Grant, P. Greenfield, A. M. Groener, S. Guest, S. Gurovich, R. Handberg, A. Hart, Z. Hatfield-Dodds, D. Homeier, G. Hosseinzadeh, T. Jenness, C. K. Jones, P. Joseph, J. B. Kalmbach, E. Karamahmetoglu, M. Kałuszyński, M. S. P. Kelley, N. Kern, W. E. Kerzendorf, E. W. Koch, S. Kulumani, A. Lee, C. Ly, Z. Ma, C. MacBride, J. M. Maljaars, D. Muna, N. A. Murphy, H. Norman, R. O'Steen, K. A. Oman, C. Pacifici, S. Pascual, J. Pascual-Granado, R. R. Patil, G. I. Perren, T. E. Pickering, T. Rastogi, B. R. Roulston, D. F. Ryan, E. S. Rykoff, J. Sabater, P. Sakurikar, J. Salgado, A. Sanghi, N. Saunders, V. Savchenko, L. Schwardt, M. Seifert-Eckert, A. Y. Shih, A. S. Jain, G. Shukla, J. Sick, C. Simpson, S. Singanamalla, L. P. Singer, J. Singhal, M. Sinha, B. M. Sipőcz, L. R. Spitler, D. Stansby, O. Streicher, J. Šumak, J. D. Swinbank, D. S. Taranu, N. Tewary, G. R. Tremblay, M. de Val-Borro, S. J. Van Kooten, Z. Vasović, S. Verma, J. V. de Miranda Cardoso, P. K. G. Williams, T. J. Wilson, B. Winkel, W. M. Wood-Vasey, R. Xue, P. Yoachim, C. Zhang, A. Zonca, and Astropy Project Contributors, The Astropy Project: Sustaining and Growing a Community-oriented Open-source Project and the Latest Major Release (v5.0) of the Core Package, *The Astrophysical Journal* **935**, 167 (2022).
 - [83] C. R. Harris, K. J. Millman, S. J. van der Walt, R. Gommers, P. Virtanen, D. Cournapeau, E. Wieser, J. Taylor, S. Berg, N. J. Smith, R. Kern, M. Picus, S. Hoyer, M. H. van Kerkwijk, M. Brett, A. Haldane, J. F. del Río, M. Wiebe, P. Peterson, P. Gérard-Marchant, K. Sheppard, T. Reddy, W. Weckesser, H. Abbasi, C. Gohlke, and T. E. Oliphant, Array programming with NumPy, *Nature* **585**, 357 (2020).
 - [84] P. Virtanen, R. Gommers, T. E. Oliphant, M. Haberland, T. Reddy, D. Cournapeau, E. Burovski, P. Peterson, W. Weckesser, J. Bright, S. J. van der Walt, M. Brett, J. Wilson, K. J. Millman, N. Mayorov, A. R. J.

- Nelson, E. Jones, R. Kern, E. Larson, C. J. Carey, Í. Polat, Y. Feng, E. W. Moore, J. VanderPlas, D. Laxalde, J. Perktold, R. Cimrman, I. Henriksen, E. A. Quintero, C. R. Harris, A. M. Archibald, A. H. Ribeiro, F. Pedregosa, P. van Mulbregt, and SciPy 1.0 Contributors, SciPy 1.0: Fundamental algorithms for scientific computing in Python, *Nature Methods* **17**, 261 (2020).
- [85] J. D. Hunter, Matplotlib: A 2D Graphics Environment, *Computing in Science and Engineering* **9**, 90 (2007).
- [86] M. Bonamigo, G. Despali, M. Limousin, R. Angulo, C. Giocoli, and G. Soucail, Universality of dark matter haloes shape over six decades in mass: Insights from the Millennium XXL and SBARBINE simulations, *Monthly Notices of the Royal Astronomical Society* **449**, 3171 (2015).